Cell Ingression and Apical Shape Oscillations during Dorsal Closure in *Drosophila*

Adam Sokolow, Yusuke Toyama, Daniel P. Kiehart, and Glenn Edwards

Supporting Material

S1 Materials & Methods

S1.1 *Drosophila* Genetics, Embryo Handling, and Microscopy

We used standard methods for preparing *Drosophila melanogaster* embryos for *in-vivo* time-lapsed microscopy with 500ms temporal resolution. Flies expressed GFP-DE-cadherin under the control of the ubiquitin promoter/enhancer cassette (12) to provide image contrast. These embryos also carried w^- at the endogenous locus for white (eyes) on the X chromosome and a w^+ mini gene marker associated with the GFP-DE-cadherin transgene but were otherwise wild type. They were collected, dechorionated, and subsequently mounted in a modified chamber between a gas-permeable membrane (Teflon) and a glass coverslip that allowed development to proceed while time-lapsed confocal images were collected (13, 14). Data sets began at early stages of dorsal closure (before the onset of zipping for three out of the five embryos) and continued for 2-4 hours at 22°C. Embryos imaged in this manner survived and hatched. Fluorescent images (488 nm excitation) were collected with spinning-disc confocal microscopy using a Yokagawa CS-10 confocal head mounted on a Zeiss Axioplan microscope. A 25x, 0.8 NA multi-immersion objective was used with immersion oil. A complete Z-scan included from 11 to 18 z-planes (in 1 micron steps), collected in between 9 and 15 seconds. This produced 600-1100 sets of z-stacks for each embryo examined.

The embryo in Fig. 1*A* images the entire dorsal surface. Imaging contrast was due to GFP-moesin (1). This image was used for heuristic purposes and was not included in any quantitative analyses.

S1.2 Segmentation Overview

We developed novel mask-projection and segmentation methods that enabled us to locate cell edges with high resolution in each three-dimensional confocal image of the dorsal surface. Implementation of these

methods is summarized below. It included the mask-projection method to address the curvature of the dorsal surface (S1.2.1) and a semiautomated segmentation method to provide quantitative measurements of cell shapes and locations in a sequence of time-lapsed confocal images (S1.2.2). At early stages of closure, complete imaging of the dorsal surface required deep z-slices which included regions of yolk that contributed unwanted fluorescence. The mask-projection method selected cell junctions in the amnioserosa from each z-slice, excluded yolk fluorescence, and then projected the three-dimensional fluorescence intensities into a two-dimensional image. The subsequent segmentation of the images was divided into two steps. First the initial projected image was assessed by a semiautomated, user-guided method to provide a "seed" for the initial image. The second step iteratively processed the rest of the projected images. The segmentation computations were done using custom software written in C++, while all other computations were performed utilizing built-in functions of MATLAB (The MathWorks, Natick, MA).

Segmentation provided quantitative measurements of cell shapes and locations with respect to time and thus provided the basis for further analyses. Cell shapes were quantified into apical area and analyzed with methods of signal processing. Here signal processing refers to a set of standard analytical tools for assessing time series data and should not be confused with biological signaling processes. Cell ingression and oscillations in cell shape were separately quantified using Fourier and other analysis techniques. Cell centroids in combination with apical areas guided studies of spatial correlations between nearest-neighbor cells and served as the foundation for investigating regional correlations within the dorsal opening. For a detailed description of the signal analysis methods, see Supplement S2.

S1.2.1 Mask-Projection Method

To optimize segmentation we developed an initial mask-projection processing step that carried out a z-projection on a stack of confocal images of the dorsal surface and excluded unwanted fluorescence from the yolk that underlies the amnioserosa. During the early stages of dorsal closure, the region of interest (includ-

ing the amnioserosa, cells of both leading edges, and additional rows of lateral epidermal cells) exhibited curvature, which moved the apical surfaces of the cells away from the vitellin envelop (that is pressed against the coverslip). Numerous z-slices were necessary to image the entire amnioserosa where the curved surface of the embryo affected the ability to segment the lateral-most cells as summarized in Fig. S1. Simple projection schemes incorporate yolk fluorescence and confound segmentation. To circumvent this complication, we implemented a preprocessing step based on a combined masking and projection method. The masking algorithm determined the appropriate range of z-slices to capture the DE-cadherin fluorescence for each amnioserosa cell in light of the curvature of the dorsal surface. In the left-hand side of Fig. S1 *A*, the central dorsal surface has been slightly flattened to account for the mounting procedure. The "eye" characterizes the perspective of the microscope. Typically 15-20 z-scans, in 1-micron steps, were collected for each embryo. For illustration purposes, the number of z-scans has been idealized in the schematic as five confocal z-slices (left-hand side, shown in green). For mid-to-late stages of closure, the junctional complexes near the apical ends of the amnioserosa cells lie almost completely in a single optical plane for this Zeiss Axioplan confocal microscope and its 25x, 0.8 NA, oil-immersion objective. Earlier in closure there was curvature in an orthogonal anteroposterior direction and there could be some slight cell-to-cell variability in the z-direction (not shown in the idealized figure). As shown in the schematic, regions of yolk that underlie the central amnioserosa cells were also imaged as the scanning depth increases. The mask-projection method essentially excluded endogenous yolk fluorescence that would degrade contrast if traditional z-projection methods were used (Fig. S1, *B* and *C*, Movies S1-2).

The core feature of any z-projection is to map the intensity profile in the z-direction to a single value for each xy-pixel. Typically a mapping can report the maximum, sum, or average values. In our application, a numerical mask transmitted regions that included DE-cadherin fluorescence and rejected regions that did not. To optimize image contrast, the mapping reported the average intensity of the region selected by the mask. In practice, DE-cadherin fluorescence was imaged within a narrow belt ($\sim$2 microns wide in the

xy-plane, ∼5 microns thick in z) that appeared several microns below the apical surface of each amnioserosa cell. We observed that the depth of the mask could change incrementally both within a cell and from cell to cell.

The overall masking process involved multiple numerical steps. As an intuitive overview, these steps were: 1) to establish a fluorescence intensity threshold ($I_{threshold}$), which in turn identified the points (x_i, y_i, z_i) of the apical edges of each DE-cadherin belt; 2) to encapsulate each of these points within a cylinder, where the union of these cylinders identified the region (volume) of interest that included DE-cadherin fluorescence and excluded yolk fluorescence; and 3) to project the three-dimensional fluorescence intensity within the region of interest into a plane. More specifically, we surveyed the image planes from the surface towards the center of the embryo (hereafter referred to as top down) to establish $I_{threshold}$ for DE-cadherin fluorescence. In the cartoon on the left-hand-side of Fig. S1A, the amnioserosa is highlighted in red. The top z-slice contains no amnioserosa tissue and thus has no suprathreshold points, while the second z-slice has a set of points within the amnioserosa that satisfy $I(x_i, y_i, z_i) > I_{threshold}$. For each of these points (x_i, y_i, z_i) in the second z-plane, we numerically constructed a cylinder. Its azimuthal axis coincided with the z-axis of the confocal microscope and was centered at (x_i, y_i). Typically the cylinder had a radius of 10 microns to capture both fluorescent cell edges and contrasting cell interiors. The height of the cylinder typically was six imaging planes (∼5-6 μm) and in practice captured the fluorescent edges associated with the DE-cadherin belt. Before iterating this process for the next (deeper) z-plane, we excluded from subsequent iterations those suprathreshold points within or below the cylinders. In practice, the top-down approach and this identification of excluded volume avoided yolk fluorescence. This process was repeated iteratively to capture peripheral DE-cadherin fluorescence corresponding to deeper z-planes. We took the union of the cylinders from all the iterative steps to determine the volume of interest and captured the overall DE-cadherin fluorescence of the amnioserosa tissue. The overall process is summarized schematically in the right-hand-side of Fig. S1A, where the ellipse and the two elliptical rings in the top three planes represent slices through the region of interest. The red

regions external to the ellipse and the elliptical rings contain no suprathreshold points, while the red regions internal to the elliptical rings represent volumes excluded by previous iterations. While the intensity of the yolk fluorescence could be comparable to that of DE-cadherin fluorescence, the two are readily distinguished due to this top-down analysis. At the conclusion of the overall masking process, the 3-D intensities were projected into a 2-D image as portrayed in the bottom plane on the right-hand side of Fig. S1*A*.

For stability of the subsequent numerical segmentation of the projected image (Supplement S1.2.2), a relatively smooth transition in fluorescence intensity was desirable. We avoided sharp transitions in fluorescence intensity at the edge of the amnioserosa that would compromise the random walk of the Monte Carlo process that was based on image gradients. To do this, we numerically added a weak fluorescent background to the region of the projected image outside of the dorsal opening.

In practice, the mask-projection method effectively excluded the endogenous yolk fluorescence and substantially improved image contrast relative to a conventional z-projection method (Fig. S1, *B* and *C*). However, there were some limitations that typify any projection method that projects into a plane. For example, the projection of a cell on a curved surface into an xy-plane introduced distortions in cell shape, in particular for the ventral most cells included in any given image. We found the left-right distortion to be less than four percent during the earliest stages of closure, while the anteroposterior distortion is less than eight percent (11). In addition, the mask projection method could be misled by image "flicker," which could compromise the z-centering of a mask and locally degrade the image contrast. Ultimately limitations due to flicker were circumvented by the segmentation method.

S1.2.2 Segmentation Method

Our overall goal was to segment (defined below) images of the amnioserosa tissue with cellular resolution in a sequence of time-lapsed confocal images. In the past, segmenting the dorsal opening from the surrounding tissue took advantage of the strong fluorescence of the supracellular purse string as labeled with GFP-moesin

(3–5, 8, 14). Edge-detection-based segmentation of individual cells was substantially more challenging due to both the varying contrast and the relatively large number of cells (segments) in an image. While the use of GFP-DE-cadherin (fluoresces at cell junctions (12)) improved contrast in the imaging of amnioserosa cell boundaries, successful segmentation required a novel and more powerful algorithm.

Before proceeding, we define some key terminology. In our application, *segmentation* refers to the process by which fluorescence intensity patterns within a confocal image were assigned to cell edges or cell interiors or was used to exclude other biological structures such as the leading edge cells. We note that segmenting a smooth and continuous DE-cadherin belt (an extended structure that spans many pixels) resulted in subpixel resolution. A *seed* is an initial starting point for an algorithm, i.e., an educated guess. The algorithm we implemented to segment amnioserosa cells required a seed segmentation, which was then iteratively refined to produce a *final segmentation*. With the exception of the initial image in a time series of confocal images, the final segmentation of the preceding image served as the seed segmentation for the subsequent image (*Active Contour Segmentation*, red box, Fig. S2). The segmentation of the initial image (not having the benefit a predecessor image) required an independent process to create its seed (*initial seeding process*, green box, Fig. S2).

We implemented a Monte Carlo minimization process as a modification to the active contour method 'snakes' for segmenting each amnioserosa cell (15). The snakes method detects image edges by energy minimization, and we based optimization of the active contour on the repeated random searches that typify a Monte Carlo method. More specifically, the original snake method considered the energy of a single loop of elastic springs, i.e., a snake, and a potential energy landscape that corresponds to the inverse of the fluorescence intensity of a confocal image. Then energy minimization results in the snake seeking out paths of bright fluorescence that correspond to wells in the inverse-intensity landscape, i.e., the DE-cadherin fluorescence in the junctions that join the lateral surfaces of adjacent cells near their apical ends (Fig. 1). In contrast, our application of the Monte Carlo method (e.g., (16)) included snaking each amnioserosa

cell repeatedly in order to refine the seed segmentation by searching xy values for snake geometries with a random walk. Indeed repeated passes of the Monte Carlo minimization to a single cell typically yielded many non-identical but quite similar candidate contours for that cell. For each pass, a random walk began with a seed segmentation and continued until the changes in energy were minimized or a maximum number of iterations was reached. Hundreds of candidate contours were then averaged together to produce an intermediate segmentation of that cell, where segmentation inaccuracies tended to cancel in the averaging process: thus the Monte Carlo process refined the image. During this iterative process, segmenting a cell included numerous consistency checks with neighboring cells (hierarchical knowledge) to improve image refinement. For example, for nearest-neighbor cells that were relatively small or skinny, the random walk was biased to avoid erroneously stepping from the edge of the cell of interest to a non-common edge of that neighboring cell. Additionally, for cells with relatively sharp edges or relatively small apical areas, the step size of the random walk was reduced to avoid both erroneous rounded edges or the erroneous collapse of a snake to zero apical area. These two examples represent segmentation failures that can occur with an Euler implicit method, e.g., the original energy minimization that the snake method implemented, or a simple Monte Carlo based method (without biased sampling) for energy minimization without hierarchial constraints.

The next step was to refine further the intermediate segmentation by addressing issues relating to cells collectively constituting amnioserosa tissue. All of the intermediately segmented cells were again further refined by pairwise comparison of neighboring cells, providing another hierarchical consistency check. More specifically, in step I of the flowchart the common boundaries between two cells were averaged to ensure consistency, resulting in the final segmentation of this confocal image. This step substantially improved our modified active contour method and resulted in a successful segmentation of amnioserosa within the dorsal opening. Following the final segmentation of one confocal image, the results were saved, cell areas were calculated, and preparations were made for the segmentation of the subsequent image (Flowchart, steps

J-L). Preparations included determining nearest neighbors, calculating each cell's aspect ratio, etc., and providing the final segmentation of the current image as the seed segmentation for the subsequent image. An inherent feature of this method is that the index of each cell was readily preserved from image to image.

To create the seed for the first image (that had no predecessor image), we developed a novel segmentation method that mimicked heat flow, which is outlined in the green box in the flowchart. While this was an artificial application of heat flow in the sense that there was no actual temperature gradient across the amnioserosa tissue, this abstraction resulted in an effective algorithm that generated a seed segmentation for the first confocal image. The initial confocal image was first enhanced by hand to achieve continuous cell edges and to exclude localized spots of fluorescent intensity. While user intervention for the approximately two hundred cells in the initial image was tedious, improving the seed segmentation of the first image brought a huge return in the subsequent segmentation process.

There were multiple steps to the seed segmentation of the first image. Step *A* in the flowchart summarizes a survey of each pixel in the mask-projected confocal image and, based on its intensity value, assigned it to be heat insulating or conducting. We chose a threshold such that bright cell boundaries were insulators and the dark centers of cells were conductors. Fig. S3 and Movie S3 visualize the key steps in this algorithm, where the confocal image to be segmented is presented in the left image of the bottom row and the progression of the seed segmentation for two cells is tracked from left to right as heat flow is stepped through 1 to 50 to 350 iterations. The challenge was to pick an image intensity threshold such that the majority of the cells were enclosed by a continuous insulating boundary, i.e., a continuous loop of DE-cadherin fluorescence, without including too much fluorescence background from the cell interior. A well-imaged cell with a continuous insulating boundary was referred to as a closed cell. Imperfections or ambiguities in the confocal images resulted in cells with gaps in the DE-cadherin fluorescence that were interpreted as "thermal" leaks between neighboring cells. We referred to such cells as leaky cells. To visualize these steps, consider the images in the left most column (iteration 1) of Fig. S3. The survey of the confocal image (lower frame) results in the

assignment of the insulating boundaries, shown as white pixels in the middle and top frames. The choice of threshold produced closed and leaky cells. For example, track the leaky (red square) and closed (blue square) cells in the lower confocal image to the middle (or top) frame.

The next step in the seed segmentation of the first image was to establish two independent, initial temperature distributions, steps B and C in the flowchart of Fig. S2. Implementation is visualized by the top and middle images of the first column in Fig. S3. One linear temperature distribution was along the AP axis (top image, iteration 1 as before) and the other was along the LR axis (middle image). First let's consider the AP direction. Having defined an initial temperature for every conducting pixel (row T_{AP}, iteration 1), we next let heat flow through the conducting pixels based on the difference in temperatures for adjacent pixels, as visualized by moving from left to right through the images of the T_{AP} row for iterations 1 to 50 to 350 of Fig. S3. We then repeated this analysis for the LR temperature difference as summarized in the T_{LR} row of Fig. S3, iterations 1 to 50 to 350. Note that before heat flows, the temperature contours are straight lines, perpendicular to the direction of the temperature gradient, and present no information about cell shapes. Moreover, initially each cell was characterized by a number of distinct temperatures. The user tracked the iterations of heat flow until outlines of the cell shapes became apparent (detailed below) and the temperature within each cell approached equilibrium. This can be seen in tracking iterations from left to right in Fig. S3 and Movie S3, where initially straight contours progressively bend to the shape of the insulating cell boundaries. As the number of iterations increased, each cell temperature became more homogeneous and when the two distributions were overlapped each cell could be distinguished.

To understand how this algorithm works in practice, it is informative to consider how this abstract heat flows in closed and leaky cells. In a closed system, with a non-uniform temperature distribution, heat flows from hot to cold regions until a uniform, equilibrium temperature is reached. During this analysis, a closed cell was thermally isolated from its neighbors and approaches its characteristic equilibrium temperature (blue cell, combined row, iteration 350 of Fig. S3). In contrast, a leaky cell with a small gap in its insulating

boundary (red cell, combined row, iteration 350 of Fig. S3) would share a conducting path with a neighboring cell as the two cells approached equilibrium. Since the gap was small, the time course to equilibrium typically was slower that what we observed in closed cells. A key was we only let heat flow until a signature of the cell shape became apparent in the temperature distribution, which occurred before reaching thermal equilibrium. The net result was a "thermal draft" between the two leaky cells (red cell and its upper left neighbor, in combined row, iteration 350 of Fig. S3).

Step E in the flowchart brings together the until now independent assessments of heat flow resulting from the initial temperature distributions in the AP (upper row) and LR (middle row) assessments. As can be seen from inspection of Fig. S3, in isolation both the AP and the LR analyses resulted in multiple cells having similar characteristic temperatures, e.g., the two orange cells in the T_{LR} row after 350 iterations. By combining the AP and LR assessments, we straightforwardly segmented the cells. The red and blue colors superimposed on the confocal images in the combined row of Fig. S3 represent the pixels corresponding to the intersection of two finite ranges of temperature (one from AP and one from LR), where the user-defined range was centered on different temperature values for each cell and each assessment. As one would expect, the intersection of the LR and AP assessments in the image presented in the combined row, iteration 1 was square since the boundaries of a cell have had insufficient time to significantly influence the temperature distribution within a cell. As the number of iterations increased, these regions of intersection grew to fill the cell interior and the periphery of this region approximated the cell shape.

The red cell highlights a strength of using this heat flow method as a guide for precise and accurate segmentation. The gap in this leaky cell was characterized by an increase in the density of contour lines, allowing two leaky cells to be distinguished in this seed segmentation. The initial segmentation of leaky cells proved accurate enough to be an effective seed, which was further refined by our active contour method that spanned the gaps and resulted in successfully segmented cells (Movie S4).

As for details of the numerical methods, we implemented standard techniques to solve the heat equation.

As reviewed in (17), we scaled "thermal" time in the abstract temperature distribution to the conductivity of the material such that a forward time-centered space-difference equation of the time-dependent heat equation became equivalent to an iterative method for solving the steady-state heat equation. We then recognized that we merely wanted to mimic heat flow and thus could numerically solve the equilibrium equation using a Gauss-Seidel over-relaxation method (17, 18). In applying the Gauss-Seidel over relaxation method, we have treated the insulating pixels with a Ghost Cell method based on a first-order difference equation representing the constraint that no heat can flow through an insulating pixel.

S1.2.3 Results of the Segmentation Method

We segmented a total of 815 cells in the five confocal stacks of embryos undergoing dorsal closure. 645 of the cells identified in the seed segmentation of the initial confocal images were segmented for a substantial number of confocal images, which corresponded to greater than ∼90 percent of the area of the dorsal opening. Segmentation of the remaining 170 cells was confounded by the lack of neighboring cells (which reduced hierarchial constraints) and by oblong cross sections or small apical areas (which were more susceptible to snake collapse during a random walk). These cells were suitable for some but not all analyses and typically were "short lived" and near one or both of the leading edges. For example, in Fig. 1*B* there is a small "island of a cell" near the anterior canthus in Fig. 1*B*. Another example is a gap between cells indicated by the arrow in Fig. 1*B*. Occasionally, a neighboring delaminating cell or other image imperfections could lead to erroneous snake points (offset from biological cell edges by distances of several microns for durations of several minutes). Less frequently, we saw false edges due to strong intracellular or extracellular fluorescence. The subsequent analyses of the segmented images were designed to be insensitive to the limitations of the segmentation process. The legend to Table S1 specifies when 815 or 645 cells were used in the statistical analyses. 645 cells were used for all of the Fourier analyses, the analysis of the relative net force, and some of the correlation analyses. 195 cells (category I) were used for other correlation analyses based on the onset

of ingression.

Numerical details for the calculation of areas and centroids are as follows. The area was calculated from a number of triangles determined by sequential snake points with a common vertex (approximately the centroid). The true centroid was calculated using weights provided by these triangles. Thus giving us both the area of cell 'i' at a specific time, $a_i(t)$, and its centroid $\overrightarrow{c_i}(t)$. An example of the output of our algorithm is shown in Fig. 1*E*, which traces the $a_i(t)$ for three cells, distinguished by three colors in Fig. 1, *B-D*.

S1.3 Fourier Analyses

Fourier analysis is a preferred method to quantify a complex waveform, for example, as a sum of sine and cosine functions. As heuristic examples, consider two waveforms. For a signal that is either a pure sine or cosine wave, the Fourier transform is characterized by a single frequency, a single amplitude, and a single phase. To generalize to more complex waveforms, the Fourier transform reports a list of sine and cosine functions (Fourier components), each characterized by a specific frequency, amplitude, and phase, such that when all of these sine and cosine functions are added together they reproduce the original waveform. Typically the more complex the waveform, the longer the list of Fourier components. Considering the frequency distribution of the Fourier components frequently leads to insights regarding the underlying mechanisms. In Supplement S3, we summarize the frequency-dependent damping that dominates the stress-strain properties of cells subject to driving forces.

A spectrogram (19) results from a sequence of Fourier transforms, each taken in a time window that is stepped throughout the duration of the data set. While typically a Fourier transform was applied to the full time course of the data trace, spectrograms allowed us to track the time dependence of Fourier components as we progressed through the data trace.

S1.4 Geometry of the Dorsal Opening

S1.4.1 Determining the Two Leading Edges

The dorsal opening is defined by amnioserosa tissue and the two surrounding leading edges of the lateral epidermis. DE-cadherin provided excellent contrast for the apical edges of the amnioserosa cells in our confocal images. However, DE-cadherin did not result in contrast for the two purse strings, unlike the predominant fluorescence of the two purse strings as we and others have observed when either actin or myosin has been labeled with fluorescent constructs (1–9, 14, 20). We determined the extent of the dorsal opening from the periphery of the segmented amnioserosa cells using the DE-cadherin fluorescence as a proxy for the leading edge. As discussed in Supplement S2.3, we successfully segmented the categories of cells (I, II, and III) in the amnioserosa throughout the time-lapsed, confocal images. The snake points from the outermost portions of the cell boundaries were used to define the extent of the dorsal opening and thus approximated the two leading edges. The snake points were then divided into two sets according to the AP axis. At early stages of dorsal closure each set was then fitted with a 4th-order polynomial to approximate the two leading edges (two thick black traces, Fig. S4*A*). As closure progressed, we found that a 2nd-order polynomial became sufficient to account for each leading edge. The two canthi correspond to the intersections of the two fitted polynomials. As discussed in S1.2.3 and S2.3, most of the cells that were not successfully segmented were near one or both leading edges, which was the major source of uncertainty in this algorithm for determining the geometry of the dorsal opening. Typically these "snake failures" occurred on small, oblong cells with their long axis lying along the periphery (Fig. 1, *B-D*), and as such, we estimated the uncertainties to be less than 3 microns for either leading edge and less than 5 microns for either canthus. It is possible that the observed oblong geometry was characteristic of the ingression of the second row of amnioserosa cells proximal to a purse string.

S1.4.2 Cell Proximity to the Two Leading Edges

Once the two leading edges were determined, it was straightforward to measure the distance from a cell centroid to either canthus, i.e., d_A or d_P for two (red, blue) cells in Fig. S4*A*. In addition, Fig. S4*A* also indicates the minimum distance from each centroid to a leading edge d_{PS}. In general, these distances were tracked throughout the confocal images or until a cell ingressed.

S1.4.3 Sub-Regions of the Dorsal Opening

Measurements of cell distances from the two canthi (d_A, d_P) and the two purse strings (d_{PS}) lend themselves to a natural geometry for regionalizing the dorsal opening. First, consider the two intersecting magenta traces in Fig. S4*B*, which are a constant distance from the leading edges. This pair of magenta traces, and the pair of thick black traces that correspond to the two leading edges, are the two isocontours (one pair corresponds to one isocontour) shown in the figure. Three additional isocontours are shown in thin black lines in Fig. S4*B*. Now consider a set of green traces, each determined by a constant value for the coordinate C, which was defined to be $\ln(d_A/d_P)$. This mathematical formula depends on the distances from the two canthi d_A and d_P and was borrowed from one of the two coordinates of a bipolar coordinate system (21). A non-zero value for C corresponds to a circular arc. In contrast, a value of $C = 0$ is realized for the symmetric case $d_A = d_P$, which corresponds to the single dashed green line in Fig. S4*B*. Isocontours corresponding to a total of seven values of C are presented in Fig. S4*B*, the three green (two thick arcs and one dashed line) and four additional isocontours (black arcs).

Five contours based on this geometrical construction were used to separate the dorsal opening into sub-regions. In practice, one isocontour was determined by taking one-fourth of the value for the maximum distance of the dorsal opening in the L-R (vertical in the figure) direction, which defined the magenta isocontour (Fig. S4*B*). Then the two intersections of the two magenta traces defined two values for C that determined the solid green isocontours (two thick green arcs). The last isocontour was the symmetric dashed-

green line. The thick black, magenta, thick green, and dashed green isocontours shown in Fig. S4*B* defined the colorized sub-regions that appear in Fig. S4*C*, Fig. S12*A*, and in the main text as Fig. 3, *A*-*C*. The subregions of the dorsal opening were defined using the initial confocal image. False colors were assigned to all the segmented cells in the dorsal opening according to the location of each cell's centroid, and then the color-classified cells were tracked throughout all subsequent confocal images.

S2 Analyses of Changes in Apical Cross-Sectional Areas

We surveyed area changes from the early-to-late stages of dorsal closure for 645 segmented amnioserosa cells exhibiting substantial durations from five embryos. A significant fraction of the segmented cells exhibited both similar and variable characteristics with respect to changes in apical area. These are summarized by the three cells in Fig. 1, the cell in Fig. 2, the three cells in Figs. S5-S7, and the two cells presented in section S4. First, there were complex oscillations, confirming previous observations (6, 7, 10). Second, these oscillations were on top of a prominent function that we describe here as a "background function." Many of these cells exhibited a background function that was shoulder shaped. However, there was some variability in the initial values for the area, the duration of its initial plateau, and the rate of ingression for these background functions. Furthermore, the amplitude of the oscillations seemed to decrease as the cell progressed through the shoulder. To quantitatively assess these characteristics, we applied analytical tools based on Fourier transforms (18, 19) to our data sets.

S2.1 Ingression Function

The analytical deconstruction of cell area as a function of time is a multistep process, so in this and the following paragraphs we provide an intuitive overview guided by specific examples before presenting detailed analytical justifications followed by a summary of numerical methods. Three illustrative cells were chosen to be in close proximity to one another (panel *A* in Figs. S5-S7). As a first step in the deconstruction, area traces

were separated into a higher-frequency contribution $a_{high,i}(t)$ and a lower-frequency contribution $a_{low,i}(t)$ (panel *B*, Figs. S5-S7), where the blue and red traces summed to the black trace in panel *A*. The second step was to fit $a_{low,i}(t)$ with a mathematical function that characterized the shoulder, i.e., an ingression function $I_i(t)$ for the i^{th} cell. The magenta trace in each panel *C* in Figs. S5-S7 are three examples of $I_i(t)$, where $a_{low,i}(t)$ from panel *B* in Figs. S5-S7 has been reproduced in blue for comparison purposes. The green trace in panel *C* in Figs. S5-S7, respectively is the lower-frequency residual, i.e., the difference between the blue $a_{low,i}(t)$ and the magenta $I_i(t)$. This highlights that this analysis was an inherently approximate method. We excluded unreliable fits from subsequent analyses as described below.

Key to this analysis was the choice for the ingression function. The generic shape for the experimental data shown in panel *A* in Figs. S5-S7 was a plateau that falls off the horizontal, i.e., a shoulder, and entered an interval of persistent area loss. Thus we required a function that fell from high to low, a parameter that specified the value of the plateau area and a parameter that specified how rapidly the area fell off. We could build $I_i(t)$ from a familiar S-shaped curve by inverting and scaling its area and, in time, scaling how rapidly and when it ingresses. There are numerous S-shaped functions that could be used as the basis for $I_i(t)$, including a complementary error function, a hyperbolic tangent function, an inverse tangent function, a logistic growth function, or the Hill equation (21, 22). We considered each of these functions and found that they produced essentially equivalent fits to the interval of persistent area loss (data not shown). While there were distinctions between the alternative S-shaped functions for periods just before and just after this interval, the differences were small relative to the lower-frequency residual (Panel *C*, Figs. S5-S7; Supplement S2.2) not captured by the analysis. We have chosen to use the hyperbolic tangent function as the basis for $I_i(t)$ as shown in the equation below (Eq. 2 in the main text):

$$I_i(t) = \frac{\alpha_i}{2}\left[1 - \tanh(\epsilon_i t - \tau_i)\right] \tag{S1}$$

Here t is time, α_i scales the area of the initial plateau, and the transition from the plateau to complete

ingression is determined by the expression in the square brackets that specifies the time of the inflection point (given by τ_i/ϵ_i) and the rate of the transition. For $\tanh(\epsilon_i t - \tau_i)$, the maximum rate of the transition occurs at the time of the inflection and has a value ϵ_i; consequently, the value for the maximum rate of $I_i(t)$ is $-\epsilon_i \alpha_i/2$.

The calculation of the maximum constriction rate presented in Table S1 was based on fitting a line through the inflection point as follows. The inflection point was determined from the dashed lines in Fig. 1*F*. The time interval of the linear fit was centered on the time of the inflection point (when the concavity changes sign). In practice, identifying the duration of a linear region was done on a cell-by-cell basis. For example, the duration of the red cell corresponded to the difference in the times at which the cell reached 90% and 10% of its initial apical area, for the green cell the 75% and 25% values were used, and for a cell with a linear background (not shown in Fig. 1) the total imaging time was used.

S2.2 Distinguishing Oscillations and Ingression

We applied frequency-domain techniques to 645 cells of categories I, II, and III (in contrast to the more stringent reliability requirements associated with the $I_i(t)$ analyses). In general, the Fourier transform of area as a function of time, $a_i(t)$, produced area as a function of frequency, $\tilde{a}_i(\omega)$, where for each frequency there was an area amplitude $|\tilde{a}_i(\omega)|$ and a phase. The analysis that follows was based on the amplitude information in the frequency domain. We also considered the Fourier transforms for $a_{low,i}(t)$ and $a_{high,i}(t)$. Fourier transforming the $a_{high,i}(t)$ (red trace in panel *B* of Figs. S5-S7) provided a quantitative assessment of the frequency distribution that underlies these complex oscillations as experimentally observed. Fourier transforming $a_{low,i}(t)$ revealed the list of Fourier components that contributed to $I_i(t)$, i.e., panel *F* of Figs. S5-S7.

It is instructive to consider in detail the results in the frequency domain in addition to the time domain, where the two domains are complementary. Panel *D* in Figs. S5-S7 presents the Fourier transform of the

time-domain data in panels A in Fig. S5-S7, similarly for panels E and B, and F and C, where the color code has been preserved throughout all frames of Figs. S5-S7. The insets to panels D-F are log-linear plots. Compare the purple curves in the time (panel C) and frequency (panel F) domains, which are complementary representations of the ingression function, to the raw data in panels A and D from Figs. S5-S7.

One key to the approximate nature of this signal analysis is the choice of the cut-off frequency that parameterizes low- and high-pass filters to identify the lower- and higher-frequency contributions. The challenge inherent in this choice of parameter is evident by comparing the blue and purple traces in panels C and F of Figs. S5-S7, where the signature for a hyperbolic tangent was dominant until about 1 mHz. After reviewing the Fourier transforms for all cells, we chose a value of 1.1 mHz as the optimum cut-off frequency for all the data sets. The separation of a data set into a blue lower-frequency contribution (less than 1.1 mHz) and a red higher-frequency contribution (greater than 1.1 mHz) is shown in panel E of Figs. S5-S7, where the blue trace was then used to determine $I_i(t)$. However, the low-pass filter did not fully resolve the ingression function from some additional lower-frequency oscillations as is explicitly revealed in panel B of Figs. S5-S7, where inspection of the purple (ingression function) and blue (lower-frequency contribution) traces reveals a lower-frequency residual (green trace) that is not present on the purple trace. This contribution from the lower-frequency residual was inherently unresolvable by a low-pass filter and, in particular, it was not a limitation due to the choice of value per se as there was no value for the cut-off frequency that would completely separate the frequencies of $I_i(t)$ from the frequencies of the oscillations. Consequently, this unresolvable lower-frequency residual was dropped in the analysis of $I_i(t)$, which typically introduced an error of 2-to-10 percent. Panel F of Figs. S5-S7 summarizes how the failure to fully resolve such a lower-frequency residual (the green trace) compared with the ingression function (purple trace) in frequency space, where we benefitted greatly from the prominent, distinctive pattern of $\tilde{I}_i(\omega)$ as was readily seen in the frequency domain.

S2.3 Goodness of Fit

We return to the issue of the 815 cells identified by the seed segmentation and track them through the subsequent analyses. Four-fifths of the cells (645 cells) were segmented for substantial durations, but the applicability of $I_i(t)$ to these cells was variable. More specifically, about one-fourth of the total cells (195 cells, category I cells) were analyzed by $I_i(t)$ and produced reliable fitting parameters ($\alpha_i,\ \epsilon_i,\ \tau_i$; as determined by a nonlinear regression) that enabled detailed comparisons between these cells. The area traces for category I cells included a period of a clear plateau and exhibited a clear and rapid transition. In contrast, another fourth of the cells (192 cells, category III cells) had data traces that were inconsistent with the motivation that led to $I_i(t)$, i.e., while these average-sized cells exhibited oscillations about a decreasing linear background, they exhibited neither an area plateau nor a distinctive transition. While there are parameters that could reproduce the linear background, it was not clear that would be a meaningful application of $I_i(t)$. Finally, almost a third of the cells (258 cells, category II cells) fell in between class I and III cells. Category II cells exhibited a portion of a plateau region relative to the duration of the transition, but also did not satisfy the analytical criteria to produce statistically reliable results for all three of the fitting parameters to warrant detailed comparisons in further analyses. More specifically, category I cells exhibited uncertainties in the fitting parameters that had an order of magnitude of 10%, while for category II cells the uncertainty in the fitting parameters increased by as much as 100%. Nevertheless to varying degrees cells in this category were consistent with the motivation for $I_i(t)$. The sum of the category I, II, and III cells, taken with the one-fifth of the cells (170 cells) identified in the segmentation that were tracked for insufficient durations by the active contour segmentation process (S1.2.2), totals 815 cells. In the following, we supplement this intuitive introduction with a more quantitative classification scheme.

We developed a quantitative method that identified those cells that produced reliable fitting parameters when modeled with $I_i(t)$. To appreciate the exclusion criteria, it is instructive to consider specific categories of cells. Some category II cells described in the previous paragraph showed a clear transition but did not

exhibit an extended plateau. Given the unavoidable lower-frequency residual (Panel *C* Figs. S5-S7), either a limited plateau or the absence of a plateau exacerbated the uncertainty in the results produced by the non-linear regression. Thus while this type of cell was consistent with the motivation for an ingression function, the application of $I_i(t)$ to this data set resulted in unacceptably large uncertainties for some or all of the fitting parameters ($\leq 100\%$). However, calculations of centroid location, maximum rates of transition, and/or initial apical areas were reliably determined since they were insensitive to the uncertainties of α_i, ϵ_i, and τ_i.

We introduced a goodness of fit parameter, γ, to quantify the categorization of cell types based on the following correlation. We found empirically that the duration of the plateau was inversely correlated to the uncertainties of α, ϵ, and τ. We defined γ by:

$$\gamma = ingression\ duration/observation\ time \tag{S2}$$

where the ingression duration was the time it took a cell to constrict from 90% to 10% of its initial apical area as determined by the fitted function $I_i(t)$ and the observation time was the experimental duration that a cell was tracked in the active segmentation algorithm (section S1.2.2). The values of γ ranged from 0.1 to 8.6, with an average of $0.89 \pm .53$. γ could be greater than one when the duration of an ingression process, as determined by the fitted $I_i(t)$, exceeded the experimental observation time. We found that cells with $\gamma \leq 2/3$ produced reliable fitting parameters (category I cells). Cells with $\gamma > 1$ were inconsistent with the $I_i(t)$ analysis (category III cells), and that cells with $2/3 < \gamma \leq 1$ fell in between (category II cells), where some cells were consistent with the $I_i(t)$ analysis but produced unacceptably large uncertainties in the fitting parameters and other cells were inconsistent with the analysis. It is important to note that frequency domain analyses also were performed in parallel with the application of $I_i(t)$ to the data sets, as described in the Supplement S2.2.

The distribution of category I, II, and III cells for each of the five embryos is presented in Fig. S8. First,

each embryo was assessed at its initial confocal image. While cells of similar categories were observed to cluster in individual embryos, we saw no overall pattern from embryo to embryo. Correlations are discussed in greater detail in section 2.2 and Supplement S4. Second, we reassessed γ to determine cell category when all the embryos were at the same stage (data not shown). This was done with reference to embryo #5, the latest staged embryo (see Table S1). More specifically, for this assessment we ignored data collected during earlier stages for embryos #1-4 so that γ was assessed at a common stage. We found that the overall distribution of γ values was worse for embryos #1-4 relative to the results shown in Fig. S8, consistent with the cells on average being at more advanced stages of ingression with reduced durations for their measured plateaus and deeper into the ingression process.

There were two principle sources of systematic error that contributed to the approximate nature of the application of the ingression function to the data sets. The first was attributable to the lower-frequency residual and the second was summarized in our discussion of the quality factor γ. In practice, cells from the three categories were well described as oscillations and an ingression process. In particular, category I cells were well described by a shoulder-shaped ingression function with reliable fitting parameters. Similarly cells of category II were consistent with a shoulder-shaped ingression function, but there was growing uncertainty ($\leq$100%) in the fitting parameters (relative to category I cells) that limited subsequent analyses. Cells of category III could be well described by a linear ingression process, where mathematically we could identify fitting parameters (α_i, ϵ_i, and τ_i) such that $I_i(t)$ was nearly linear during the observation time.

The numerical details for the signal analyses are described here and at the end of Supplement S4. The low-pass filter was a finite impulse response based on a Bohman window (301 points), implemented with MATLAB's 'filtfilt' function using a cutoff frequency of 1.1 mHz (for a discussion on windows and filtering see, for example, reference (19)). We fitted the lower frequencies of the filtered signal using MATLAB's 'nlinfit,' a nonlinear least squares routine. The higher-frequency residuals were obtained by applying the complementary high-pass filter, also based on a Bohman window. Typically, a period of an oscillation was

sampled by 10-20 data points, well above the Nyquist limit.

S3 Oscillations/Ingression Model

We now describe the oscillations/ingression model that accounted for how active contractile forces, passive elastic restoring forces, and the viscous drag are related to the cell-shape changes as measured by $a_i(t)$. This oscillations/ingression model provided a time-dependent approximation for the forces that drive area changes. We found that in general the higher-frequency oscillations were largely reversible and that the decrease in apical cross-sections for amnioserosa cells was accounted for by a family of systematic ingression processes.

The amnioserosa cells that we have investigated were in a low-Reynolds number environment, where observed velocities were attributable to unbalanced applied forces (23). Thus the edges and nodes of the amnioserosa cells only moved when there was a local imbalance in the applied forces. We have extended Purcell's insights to the classic treatment of an overdamped, driven oscillator to develop a heuristic, dynamical model that directly applied to our experimental measurements of $a_i(t)$. As shown below, this allowed us to correlate these applied forces to the rate of change of cell areas with respect to time, i.e., $\frac{da_i}{dt}$.

The actomyosin cytoskeleton within the amnioserosa cells (subapical cortical ring and the apical-medial network) are well approximated as a two-dimensional meshwork in the dorsal opening. Both the subapical cortical ring and the apical-medial network are contractile and, in addition, have elastic properties. The subapical cortical ring produces a tension that acts along the boundary of a cell. The apical-medial network has been observed to assemble and disassemble, resulting in the formation of transient chords that extend across the apical cap of the cell and produce forces that act on adherens junctions. The resultant motions are thus likely to be similar to driven, anisotropic longitudinal waves in the dorsal surface, albeit overdamped.

Contrast in our images was due to GFP-DE-Cadherin, where we have resolved fluorescent boundaries but have only partial information about local strain. We tracked displacements of this boundary but did

not resolve any flow of material within this boundary. We modeled the net forces acting on the DE-cadherin belts and resulting in radial displacement.

Consider an infinitesimal segment of the DE-Cadherin belt and associated plasma membrane of a cell. The model we propose includes elastic forces due to the membrane, the extracellular matrix and the cell cortex that we quantified with Hooke's Law. Since we have a moving boundary with fluid on either side, we modeled the damping forces due to viscosity in the form of Stoke's Law. We applied Newton's second law to our infinitesimal segment of boundary and obtained the following equation:

$$\lambda \ddot{r}(\theta,t)ds = -kr(\theta,t) - b\dot{r}(\theta,t) + f(\theta,t) \tag{S3}$$

Here λ is a line density in the inertial term $\lambda\ddot{r}(\theta,t)$, k is Hooke's constant, and $b\dot{r}(\theta,t)$ is the viscous drag. $f(\theta,t)$ is the net, time-dependent driving force acting on the boundary in the radial direction that arises from forces that were both internal to the cell and from a neighboring cell. Applying the low-Reynolds number constraint and solving for $b\dot{r}(\theta,t)$, Eq. S3 became:

$$b\dot{r}(\theta,t) = -kr(\theta,t) + f(\theta,t) \tag{S4}$$

Integrating this equation along the boundary we found:

$$\int b\dot{r}(\theta,t)ds = \int -kr(\theta,t)ds + \int f(\theta,t)ds \tag{S5}$$

The arc length ds, in polar coordinates, is given by:

$$ds = r\sqrt{1 + \left(\frac{\frac{dr}{d\theta}}{r}\right)^2}\, d\theta \tag{S6}$$

Since $\frac{dr}{d\theta}$ was much less than r until $a_i(t)$ was very small, $(\frac{dr}{d\theta}/r)^2$ was inconsequential until the end of

ingression. We thus took $ds \approx r d\theta$ and for simplicity in the following present $r(\theta, t)$ as r, etc. This resulted in the following integral around the periphery of the cell:

$$\int b\dot{r} r d\theta = \int -kr^2 d\theta + \int f r d\theta \tag{S7}$$

We exchanged the order of differentiation and integration in the term on the left-hand-side. Recognizing that $\frac{1}{2}\frac{d}{dt}\left(r^2\right) = r\dot{r}$, we found:

$$\frac{1}{2}\frac{d}{dt}\int br^2 d\theta = -\int kr^2 d\theta + \int f r d\theta \tag{S8}$$

We next considered each of three integrals independently in a mean-field approximation. We defined:

$$b_{eff}\dot{a}(t) = \frac{1}{2}\frac{d}{dt}\int br^2 d\theta \tag{S9a}$$

$$k_{eff}a(t) = \int kr^2 d\theta \tag{S9b}$$

$$f_{eff}(t) = \int f(\theta, t) r d\theta \tag{S9c}$$

Here $b_{eff}\dot{a}(t)$, $k_{eff}a(t)$, and $f_{eff}(t)$ are each spatially averaged, generalized forces. Making these substitutions into Eq. S8 we arrived at the following:

$$b_{eff}\frac{d}{dt}a(t) = -k_{eff}a(t) + f_{eff}(t) \tag{S10}$$

This is a first-order, linear differential equation with an inhomogeneous driving term $f_{eff}(t)$ that is of the same mathematical form as that of a driven harmonic oscillator in the overdamped limit of low-Reynolds number. We refer to the inhomogeneous driving term as a generalized force because it resulted from the integration of many subcellular forces acting along the periphery of a cell (Eq. S9c). For ease of presentation, in the following we set $b_{eff} = b$, and $f_{eff} = f$.

$$b\frac{da(t)}{dt} = f(t) - k_{eff}a(t) \tag{S11}$$

The term on the left-hand side of Eq. S11 accounts for viscous drag. The first term on the right-hand side is a sum of all the active contractile forces. The second term on the right-hand side is a passive elastic restoring force. As is shown below, this treatment proved adequate for investigating the frequency dependence of $f(t)$ in a viscoelastic tissue at low-Reynolds number. This equation could be applied to each cell, indexed by the subscript i, to reproduce Eq. 4. Anticipating a Fourier transform, we rewrite Eq. S11 as Eq. S12.

$$\frac{f(t)}{b} = \frac{k_{eff}}{b}a(t) + \frac{da(t)}{dt} \tag{S12}$$

We evaluated the Fourier transform of Eq. S12 and obtained the following expression for the Fourier amplitudes:

$$|\tilde{a}(\omega)| = \left[\frac{1}{b\sqrt{\left(\frac{k_{eff}}{b}\right)^2 + \omega^2}}\right] |\tilde{f}(\omega)| \tag{S13}$$

Where $\tilde{a}(\omega)$ is the Fourier transform of $a(t)$ and $\tilde{f}(\omega)$ is the Fourier transform of $f(t)$. The bracketing vertical lines in Eq. S13 indicate magnitudes, where $\tilde{a}(\omega)$ and $\tilde{f}(\omega)$ are in general complex. The expression in the square brackets on the right hand side of the equation is a transfer function that, in frequency space, relates forces to areas. Thus the transfer function directly accounted for the viscoelastic tissue through b and k_{eff}. The area $a(t)$ for a typical cell is shown in Fig. S9*A*, which is reproduced from Fig. 2*A*, with its corresponding Fourier transform $|\tilde{a}(\omega)|$ in Fig. S9*B*. The fitting process is summarized in the inset to Panel *B*, where in this $\log\left[|\tilde{a}(\omega)|\right]$ versus $\log[\omega/2\pi]$ plot the data are well approximated by a straight line of slope -1 and intercept $\log\left[|\tilde{a}(\omega = 0)|\right]$. Note that the transfer function includes the ω^{-1} dependence (attributable to the viscosity term), as can be seen by rewriting Eq. S13 for non-zero frequencies:

$$\log\left[|\tilde{a}(\omega)|\right] = -\log\omega + \log\left[\frac{|\tilde{f}(\omega)|}{b}\right] - \frac{1}{2}\log\left[\left(\frac{k_{eff}}{\omega b}\right)^2 + 1\right] \tag{S14}$$

Fitting this equation to the 645 cells of categories I, II, and III, we found that the values for k_{eff}/b ranged from $\sim$ 0.01-to-0.1 mHz. In addition, the fitting process utilized f_0, a constant (independent of ω), through the expression $|\tilde{f}(w)| = f_0 + f_1(\omega)$. Thus $|\tilde{f}(w)|/f_0 = 1 + f_1(\omega)/f_0$, accounting for the background in Fig. 2, *D* and *E*. The fitted value for f_0/b was $0.03 \pm 0.01 \mu m^2/s$. Note that $f_0 = k_{eff}|\tilde{a}(\omega = 0)|$. While uncertainties in determining values of k_{eff}/b introduced uncertainties in the magnitude of the transfer function, they do not alter the distribution of the Fourier frequencies.

Benefitting from the numerical determination of k_{eff}/b and f_0/b, we could calculate $f(t)/f_0$ from the experimental data $a(t)$, e.g., Fig. S9*A*. To see this, multiply Eq. S12 by b/f_0 and solve for $f(t)/f_0$:

$$\frac{f(t)}{f_0} = \frac{b}{f_0}\left(\frac{da(t)}{dt} + \frac{k_{eff}}{b}a(t)\right) \tag{S15}$$

The ratio of $f(t)/f_0$ is a dimensionless (unitless) force scaled by the constant f_0. Fig. 2*B* was determined using Eq. S15. The largest uncertainty in Eq. S15 was due to k_{eff}/b, which had its greatest effect when $\frac{da(t)}{dt} = 0$. Fig. S9*C* plots $f(t)/f_0$, where the inset expands the time interval from 90 to 210 seconds to summarize the overall uncertainty in the calculation.

The calculation of $|\tilde{f}(w)|/f_0$ followed from Eq. S13 where:

$$\frac{|\tilde{f}(\omega)|}{f_0} = \left[\frac{b}{f_0}\sqrt{\left(\frac{k_{eff}}{b}\right)^2 + \omega^2}\right]|\tilde{a}(\omega)| \tag{S16}$$

Equations S15 and S16 were reproduced with explicit subscripts i as Eqs. 5 and 6 in the main text, respectively. Equation S15 was applied to the full time series to produce Fig. 2, *D* and *E* and Fig. S12, *C-E*. For the evaluation of spectrograms (Fig. 2, *F* and *G*), however, each window in time corresponded to a convolution in Fourier space. Furthermore, stepping the window through time (travelling) corresponded to

convolving an iteratively phase-shifted function. More specifically, we applied a Hann window function (19) of duration $W = 1300$s (about a tenth of a typical data trace).

Fig. S10 reproduces Fig. $2G$ with an expanded false color scale. While Fig. $2G$ does not have the dynamic range in false colors to resolve the blue streak, its significance is apparent in Fig. S10.

The numerical evaluation of a derivative, specifically $\frac{da_i}{dt}$ in Eq. S15, can be challenging. The inset to Fig. S9A indicates that the data for $a_i(t)$ are not sparse and the following methods are reliable. To calculate the derivative we implemented an 11-point time-centered difference equation. A low-pass filter was applied before the numerical derivative was taken with a cutoff frequency of $17.5mHz$. Comparing our 11-point derivative to a 13-point method revealed less than 0.1% change in the calculated force. Fig. $2C$ was determined using a boxcar travelling average with a width of 1000 seconds to filter out the band of oscillations above $1mHz$.

S4 Correlation Analyses

Fig. S11 quantified the relationship between $a_{high,i}(t)$ and $a_{low,i}(t)$ in Fig. 1, *F-I* and $a_i(t)$ in Fig. 2. Fig. S11, A and B presented cells with linear ($a_{low,1}(t)$) and shoulder shaped ($a_{low,2}(t)$) backgrounds, respectively. The corresponding higher-frequency oscillations for these cells were shown in Fig. S11C ($a_{high,1}(t)$) and Fig. S11D ($a_{high,2}(t)$). The average value $\hat{a}_{low,i}(t)$ and an average amplitude envelope $\hat{a}_{high,i}(t)$ were calculated at regular intervals and appeared as diamonds in panels A and C and as open circles in panels B and D, where the mathematical method for calculating the averages based on a travelling window is presented at the end of this section (see Eqs. S17a and S17b). Fig. S11E assessed any correlation by plotting $\hat{a}_{low,i}(t)$ versus $\hat{a}_{high,i}(t)$ for all the segmented cells for this embryo. The entire data set exhibited a good linear correlation ($r^2 = 0.74$). There was a knee in the data near the origin; however, the data set was not robust enough for reliable interpretation. On the other hand, the data indicated that relatively large amnioserosa cells exhibited disproportionately large average amplitudes $\hat{a}_{high,i}$. Nonetheless, it was interesting that the

average amplitudes of higher-frequency oscillations were linearly correlated with the average areas of the lower-frequency background for all cells in categories I, II, and III.

More generally, we searched for potential correlations in cell kinematics, neighboring cells, and between cells and either a leading edge or a canthus. Our analyses failed to demonstrate a correlation between the higher-frequency oscillations and the onset of ingression, even though higher-frequency oscillations during the plateau generally preceded ingression and the average amplitude of oscillations correlated with the average cell area (additional conclusive correlations are discussed in sections 2.4, and 2.3). More specifically, we searched for additional correlations and found none as follows. 1) In isolated cells, we found no correlation between the parameters of $I_i(t)$ and the Fourier components of the higher-frequency oscillations. Such a correlation would have implied the higher-frequency oscillations regulate the onset of ingression. 2) In neighboring cells, we found no correlation in the onset of ingression and the Fourier components of the higher-frequency oscillations. Such a correlation would have implied that neighboring cells regulate the onset of ingression. 3) We found a correlation between the time at which cells complete ingression and their proximity to either the leading edge or a canthus (see section 2.3; numerical uncertainty prevented a correlation analysis based on the onset of ingression). This correlation implies that the leading edge regulates ingression. We cannot rule out the possibility that additional correlations may be drawn out by alternative analyses or that correlations may become apparent when considering silent-shape changes (see Discussion); however, our techniques should have been sensitive to any robust correlation between oscillations that resulted in area changes and the onset of a rapid decrease in apical area.

An average oscillation amplitude was calculated using a method based on the absolute value of the areas and a travelling window in time. More specifically, Eq. S17a produced an average amplitude of the higher frequency signal, $a_{high,i}(t)$, i.e., the higher-frequency oscillations. Equation S17b was a similar averaging process for the lower-frequency signal, $a_{low,i}(t)$. $w(t;t_0)$ is a Hann window function, with W=1300s, as was

used in the calculation of the spectrogram.

$$\hat{a}_{high,i}(t_0) = \frac{1}{W}\int_{t_0-W/2}^{t_0+W/2} w(t;t_0)|a_{high,i}(t)|dt \tag{S17a}$$

$$\hat{a}_{low,i}(t_0) = \frac{1}{W}\int_{t_0-W/2}^{t_0+W/2} w(t;t_0)|a_{low,i}(t)|dt \tag{S17b}$$

Numerical integration was performed using a Composite Simpson's Method (18).

S5 Region Specific Behaviors

We investigated whether cell kinematics and dynamics exhibited localized, region-specific behaviors. Fig. S12*A* plotted the area for each region of the dorsal opening as a function of time, where the color of each trace matched that of the region (the number of cells in each region is discussed in the following paragraph). Due to the geometric construction that regionalizes the dorsal opening, at time zero the two poles/canthi regions were the smallest, the areas of the two central regions were the largest, and the areas of the four peripheral regions fell in between. As closure progressed, there was a decrease in regional areas as the apical cross-sectional area of individual cells decreased until the cell completed the ingression process, which also decremented the number of cells in a region. While individual cells changed shape in time and there was junctional remodelling when cells ingress, there was relatively little mobility of amnioserosa cells from one colored region to another during dorsal closure (e.g., Fig. S12, *A*-*C*). Ideally the regionalization process should produce similar values for symmetric regions (dark blue and brown canthus regions; yellow and green interior regions; and cyan, blue, red, and orange peripheral regions) within the dorsal opening. In practice, however, the classification scheme was based on cell centroids, which introduced some non-ideality in the initial areas as centroids fell on one side or the other of lines of regional demarcation due to the asymmetry of the dorsal opening and sampling (see Supplement S1.4, Fig. S4). This effect was particularly evident in

the green and yellow interior regions, which included the largest cells of the dorsal opening. Indeed as cell size decreased with time, these two interior regions exhibited more comparable regional areas, starting at ∼5000s (Fig. S12A). This suggested that categorizing the regions of cells based on the first confocal image was a reasonable analytical strategy.

We then followed the completion of the ingression process by tracking the number of cells in each region as shown in Fig. S12B and found region-specific behavior. There were interesting asymmetries for the two interior regions. First, the average initial size of the amnioserosa cells in the posterior (green) interior was 290^{+40}_{-40} μm^2, while that of the anterior (yellow) was 210^{+70}_{-30} μm^2 (p=0.005). Second, relatively few cells completed ingression in the posterior and anterior interior regions before 12,500s and 7500s respectively (see yellow and green traces in Fig. S12B). In contrast, the pole/canthus and peripheral regions were more symmetric. In particular, the traces for the two pole/canthus regions (dark blue and brown) essentially overlapped, as do the traces for the four peripheral regions (cyan, red, blue, and orange). When region specific delays were taken into account, however, we observed comparable rates for completing ingression in each of the regions. The rates of completing the ingression process for the two canthi regions during the time interval ∼0-5000s compared favorably with the rates for the four peripheral regions during the time interval ∼7000-14000s. As for the interior regions, the rate for completing the ingression process compared favorably with that seen in the other six regions after ∼7500s for the anterior interior (yellow) region and after ∼12,500s for the posterior interior (green) region.

Fig. S12B plotted the number of cells in each region as a function of time. More importantly, panel C revealed that in addition to the complete ingression of all the cells near the two canthi regions, there was a substantial reduction in the number of cells near the periphery and away from the canthi (blue, cyan, red and orange regions). In contrast, there was markedly less ingression during closure within the interior regions (yellow and green).

In order to investigate any regional variability in the driving forces $|\tilde{f}(\omega)|/f_0$ we carried out a region-

by-region Fourier analysis as shown in Fig. S12, *C-E*. We calculated the Fourier transform $|\tilde{f}(\omega)|/f_0$ using Eq. 6 for the area as a function of time, $a_i(t)$, for each cell and then averaged the results region by region, i.e., we added the Fourier transforms for cells in the same color category and then divided by the number of cells in that category at the initial time. Fig. S12, *C-E* shows that in the two interior regions there were relatively large forces at lower frequencies (Fig. S12*C*), whereas in the four peripheral regions there were relatively smaller forces at higher frequencies (Fig. S12*D*). In addition, the smallest cells were in the two pole/canthus regions (Fig. S12*A*), which had the smallest average Fourier amplitudes (Fig. S12*B*) and the smallest average values for f_0/b (listed in the legend to Fig. S12). Thus we found that the average components of the driving force scaled with the cell size, consistent with the correlation presented in Fig. S11*E*. This suggested a constant density of force producing units that scale linearly with the apical cross sectional area.

S6 Geometric and Kinematic Measures of Amnioserosa Cells

Table S1 summarizes the results of the geometric and kinematic analyses of five segmented embryos. The initial apical areas exhibited a range of values. Typically there were concentrations of small cells near the poles/canthi, and narrow cells along the periphery, where the majority of the large cells were concentrated in the interior of the dorsal opening (Fig. 1*B*). We investigated five embryos (summarized in Table S1) where the average (mean) initial cell area is 120 ± 20 μm^2. We started imaging each of the five embryos at early-to-mid stages of dorsal closure and followed them until the end stages. Imaging for three of the five embryos began before any signs of zipping. Imaging for Embryos 4 and 5 began at a slightly later stage relative to Embryos 1-3. Comparing the values for the average cell sizes (column *B*) suggests a stage dependence.

Fig. 1*E* shows $a_i(t)$ for three cells during closure, where $a_{low,i}(t)$ for each cell is shown in panel *F*. These cells exhibit a relatively rapid rate of apical constriction and inspection of the dashed lines in Fig. 1*F* indicate the maximal constriction rate occurs near 3500s, 5000s, and 8000s for the red, green, and blue cells,

respectively (Table S1 reports calculated maximum constriction rates for all of the cells). Regardless of the staging of the embryos, we find a similar distribution of maximum constriction rates. The average value for the maximum constriction rate is 1.5 ± 0.2 $\mu m^2/minute$ (N=5 embryos).

S7 Emergent Parameter of the Setting-Sun Model

Here we compare analytical and empirical expressions for the geometry of the dorsal opening to account for a constant of proportionality presented in Table S1 and discussed in section 2.4 of the main text. The analytical equation was derived by expressing the area of the dorsal opening in terms of the canthus-to-canthus distance W and, in the perpendicular direction, the distance of the maximum opening H (Fig. S13*B*). This setting-sun model is an idealization of the dorsal opening, where the opening is defined by the area between two intersecting circular arcs as shown in Fig. S13*B*. The circles are taken to have the same radii denoted by the parameter r. Within the setting sun model, the progression of dorsal closure in time corresponds to pulling the centers of the two circles apart at a constant rate to reduce the area of the dorsal opening while maintaining the curvature ($\kappa = 1/r$) of the arcs. This model has been shown to be a good approximation from the mid-to-late stages of closure (3, 4, 8).

We define the half width w to be $\frac{W}{2}$, and half height h to be $\frac{H}{2}$, which are the semi-major and semi-minor axes of the eye-shaped dorsal opening. The angle θ is swept out from the symmetry axis to one of the canthi. For this geometry, the following relationships hold:

$$h = r(1 - \cos\theta) \tag{S18a}$$

$$w = r\sin\theta \tag{S18b}$$

It was straightforward to first calculate the area of one-half of the dorsal opening as indicated by the shading. The area of the "piece of the pie" swept out by 2θ is θr^2. Subtracting the area of the underlying triangle

resulted in the shaded region in Fig. S13. Multiplying by two, we found the expression for the area A of the entire dorsal opening to be:

$$A = 2\left[\theta r^2 - \frac{1}{2}(2w)(r-h)\right] \tag{S19}$$

Solving Eqs. S18a and S18b for r, we then made judicious substitutions into Eq. S19. More specifically, there are two terms in the square brackets in Eq. S19. For the first term, there are two powers of r, where one was replaced by the quantity that follows from Eq. S18a and the other was replaced by the quantity that follows from Eq. S18b. Completing the substitutions, we derived:

$$A = 2\left[\theta(\frac{w}{\sin\theta})(\frac{h}{1-\cos\theta}) - (w)(\frac{h}{1-\cos\theta} - h)\right] \tag{S20}$$

$$= 2\left[\frac{\theta - \sin\theta\cos\theta}{\sin\theta(1-\cos\theta)}\right] hw \tag{S21}$$

For the values of θ that correspond to dorsal closure ($\sim \pi/4$ to 0), the terms preceding hw on the right hand side of Eq. S21 had values that ranged from 2.67 to 2.75. These values varied by less than 2% of the average value 2.70, which was calculated by taking the integral of the terms in the square brackets in Eq. S21 with respect to θ from $\theta = 0$ to $\theta = \pi/4$, then divided by $\pi/4$. This theoretical variability was less than the three percent biological variability as indicated in Table S1. Thus Eq. S21, as applied to dorsal closure, implies that the area A is linearly related to the product hw to a very good approximation. Thus the average theoretical value (2.70) for the constant of proportionality compared favorably with the value 2.76 ± 0.09, i.e., the average of the experimental values (A/hw) for the five embryos as reported in column I (Table S1).

References

[1] Kiehart, D., C. Galbraith, K. Edwards, W. Rickoll, and R. Montague. 2000. Multiple forces contribute to cell sheet morphogenesis for dorsal closure in Drosophila. *Journal of Cell Biology*. 149:471.

[2] Jacinto, A., S. Woolner, and P. Martin. 2002. Dynamic Analysis of Dorsal Closure in Drosophila:: From Genetics to Cell Biology. *Developmental Cell*. 3:9–19.

[3] Hutson, M., Y. Tokutake, M. Chang, J. Bloor, S. Venakides, D. Kiehart, and G. Edwards. 2003. Forces for morphogenesis investigated with laser microsurgery and quantitative modeling. *Science*. 300:145.

[4] Peralta, X., Y. Toyama, M. Hutson, R. Montague, S. Venakides, D. Kiehart, and G. Edwards. 2007. Upregulation of forces and morphogenic asymmetries in dorsal closure during Drosophila development. *Biophysical Journal*. 92:2583–2596.

[5] Toyama, Y., X. Peralta, A. Wells, D. Kiehart, and G. Edwards. 2008. Apoptotic force and tissue dynamics during Drosophila embryogenesis. *Science*. 321:1683.

[6] Blanchard, G., S. Murugesu, R. Adams, A. Martinez-Arias, and N. Gorfinkiel. 2010. Cytoskeletal dynamics and supracellular organisation of cell shape fluctuations during dorsal closure. *Development (Cambridge, England)*. 137:2743.

[7] Solon, J., A. Kaya-Çopur, J. Colombelli, and D. Brunner. 2009. Pulsed forces timed by a ratchet-like mechanism drive directed tissue movement during dorsal closure. *Cell*. 137:1331–1342.

[8] Peralta, X., Y. Toyama, D. Kiehart, and G. Edwards. 2008. Emergent properties during dorsal closure in Drosophila morphogenesis. *Physical Biology*. 5:015004.

[9] Franke, J., R. Montague, and D. Kiehart. 2005. Nonmuscle myosin II generates forces that transmit tension and drive contraction in multiple tissues during dorsal closure. *Current Biology*. 15:2208–2221.

[10] Fernández, B., A. Arias, and A. Jacinto. 2007. Dpp signalling orchestrates dorsal closure by regulating cell shape changes both in the amnioserosa and in the epidermis. *Mechanisms of Development*. 124:884–897.

[11] Sokolow, A. 2011. Biophysical investigation of cell oscillations and ingression in tissue dynamics. PhD dissertation. Duke University, North Carolina. Department of Physics.

[12] Oda, H. and S. Tsukita. 2001. Real-time imaging of cell-cell adherens junctions reveals that Drosophila mesoderm invagination begins with two phases of apical constriction of cells. *Journal of Cell Science*. 114:493.

[13] Kiehart, D., R. Montague, W. Rickroll, D. Foard, and G. Thomas. 1994. High-resolution microscopic methods for the analysis of cellular movements in Drosophila embryos. *Methods Cell Biol*. 44:507–32.

[14] Kiehart, D., Y. Tokutake, M. Chang, M. Hutson, J. Weimann, X. Peralta, Y. Toyama, A. Wells, A. Rodriguez, and G. Edwards. 2006. Ultraviolet Laser Microbeam for Dissection of Drosophila Embryos.

[15] Kass, M., A. Witkin, and D. Terzopoulos. 1988. Snakes: Active contour models. *International Journal of Computer Vision*. 1:321–331.

[16] Pang, T. 1997. An introduction to computational physics. Cambridge University Press.

[17] Haberman, R. 2004. Applied partial differential equations: with Fourier series and boundary value problems. Pearson Prentice Hall.

[18] Burden, R. and J. Faires. 2001. Numerical Analysis. Brooks/Cole.

[19] Stearns, S. 2003. Digital signal processing with examples in MATLAB. CRC.

[20] Homsy, J., H. Jasper, X. Peralta, H. Wu, D. Kiehart, and D. Bohmann. 2006. JNK signaling coordinates integrin and actin functions during Drosophila embryogenesis. *Dynamics*. 235:427–434.

[21] McQuarrie, D. 2003. Mathematical methods for scientists and engineers. University Science Books.

[22] Cantor, C. and P. Schimmel. 1980. Biophysical Chemistry: Techniques for the study of biological structure and function. WH Freeman & Co.

[23] Purcell, E. 1977. Life at low Reynolds number. *American Journal of Physics*. 45:11.

Column:	A	B	C	D	E	F	G	H	I	J
	Initial Area (μm^2)				Max Constriction Rate ($\mu m^2/minute$)		Ingression Rate ($cells/minute$)		Area: Constant of Proportionality	
	Dorsal Opening	Individual Cells		Duration ($minutes$)						
#		mean	(min/max)		mean	(min/max)	Rate	r^2	Slope	r^2
1	24,210	122^{+71}_{-70}	(1/339)	243	$1.2^{+1.7}_{-0.5}$	(0.2/7.9)	0.80	0.995	2.83	0.995
2	23,210	129^{+74}_{-73}	(11/323)	222	$1.8^{+4.5}_{-1.0}$	(0.4/12.0)	0.77	0.994	2.87	0.998
3	19,501	136^{+73}_{-76}	(5/409)	234	$1.4^{+3.6}_{-0.7}$	(0.2/13.6)	0.59	0.995	2.74	0.999
4	15,773	97^{+65}_{-52}	(14/304)	145	$1.5^{+2.5}_{-0.7}$	(0.3/9.1)	1.09	0.994	2.65	0.993
5	13,105	106^{+67}_{-61}	(18/265)	122	$1.7^{+1.3}_{-0.7}$	(0.6/4.7)	0.91	0.997	2.71	0.993

TABLE S1. Geometric and kinematic characterization of the dorsal opening and amnioserosa cells. The first column identifies each embryo by number. Columns *A*-*C* report the areas of the dorsal opening and the amnioserosa cells (mean and range). Column *D* reports the imaging time, where each embryo was tracked until the end stages of closure. Columns *E* and *F* report the maximum constriction rate (mean and range) for the ingression process. Column *G* reports the average rate that the population of cells complete ingression, i.e., "ingression rate." Column *H* reports the corresponding r^2 values for the linear fitting process. Columns *I* and *J* report a constant of proportionality and corresponding r^2 value for a geometric analysis of the dorsal opening as discussed in section 2.3 and Supplement S1.4. Typically statistics were determined from 201, 182, 144, 162 and 126 cells (totalling 815 cells) for the five embryos. However, statistics for the maximum constriction rate were restricted to a subset of the segmented cells (see section 2.1, Supplement S2 and S7) and were determined from 166, 147, 123, 115, and 94 cells, respectively (totalling 645 cells).

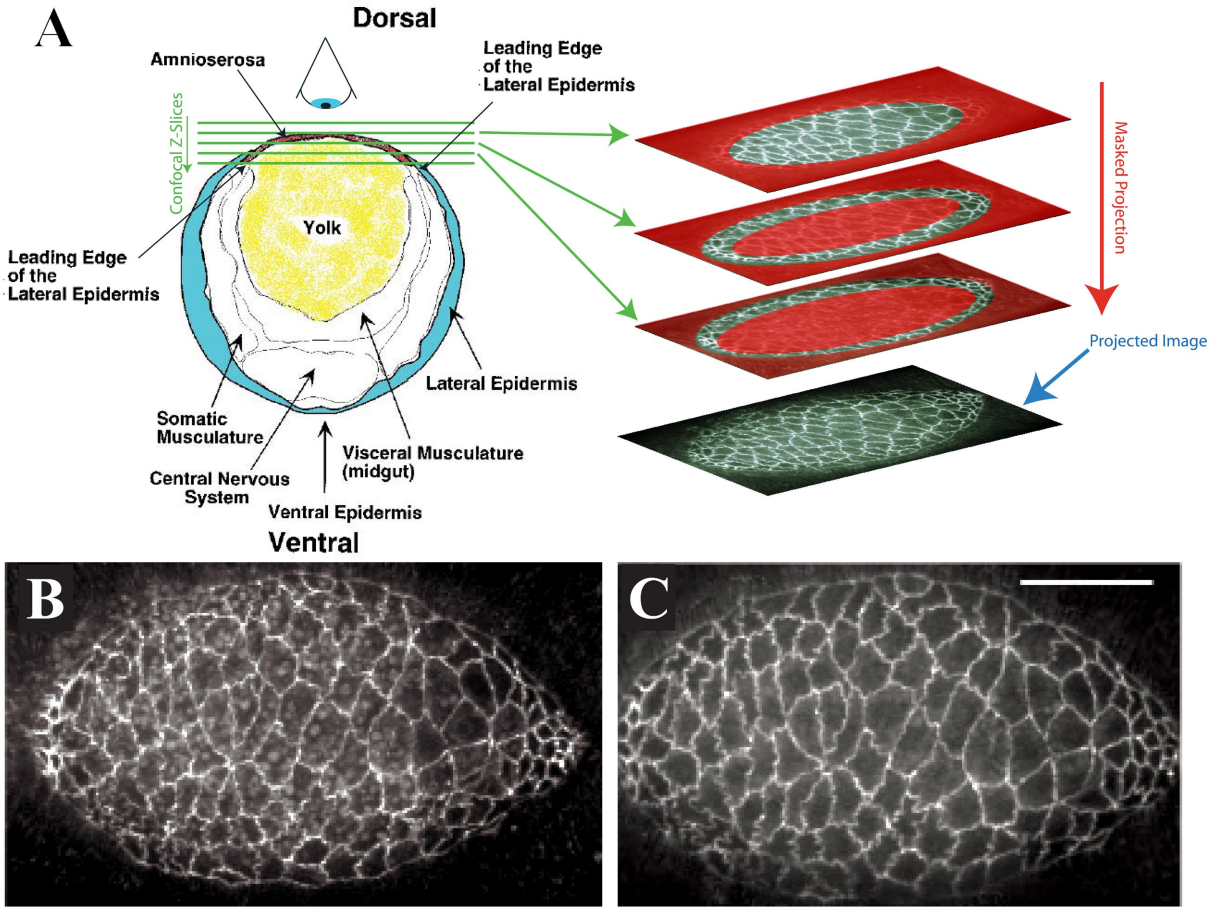

FIGURE S1. Mask Projection Method. A: on the left, schematic summarizing confocal imaging of the dorsal surface of a *Drosophila* embryo. This is a transverse section taken through the middle (along the A-P axis) of the dorsal opening (Cartoon adapted from (1)). On the right, three confocal images (as indicated by the green arrows) are projected into the x-y plane (projected image). The number of confocal slices has been idealized for presentation purposes (Supplement S1.2.1). B: A conventional z-projection method (mean) exhibiting both DE-cadherin fluorescence and globular yolk fluorescence. C: Masked-projection method, where the scale bar is 50 μm.

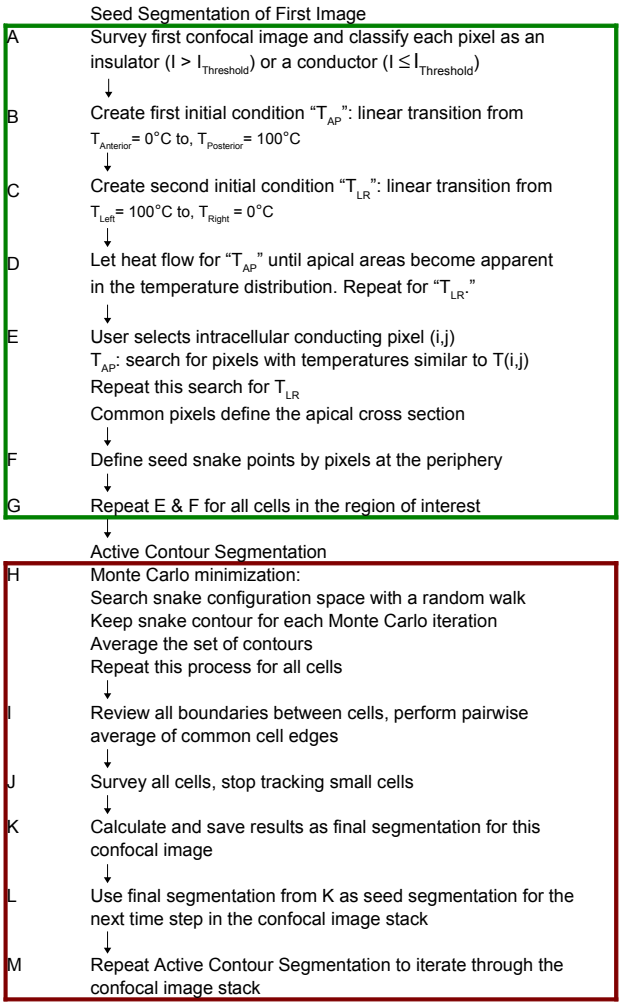

FIGURE S2. Flowchart of the Segmentation Algorithm: Steps *A*-*G* are the Seed Segmentation of the First Image of the confocal stack using a method which mimics heat flow. Step *A*: a threshold intensity is chosen so that most cells form closed loops of fluorescence. Steps *B* and *C*: perpendicular initial conditions are established independently so that heat can flow in Step *D*. Steps *E*-*G*: cells are defined by the intersections of common temperature regions from both heat flows. The periphery of these pixel sets is the seed snake for Step *H*. Steps *H*-*M* are the Active Contour Segmentation method for the entire stack. Step *H*: each snake contour has an energy that must be minimized before it becomes representative of the confocal image. We implement a Monte Carlo scheme to minimize these energies. Step *I*: prior steps dealt only with cells individually, here we implement consistency checks with neighboring cells (hierarchical knowledge). Steps *J* and *K*: calculate geometrical values for each cell, determine cells that are too small (nearly completely ingressed) and are no longer tracked, and update nearest-neighbor assignments. Steps *L* and *M*: These steps set up the next iteration of the active contour segmentation.

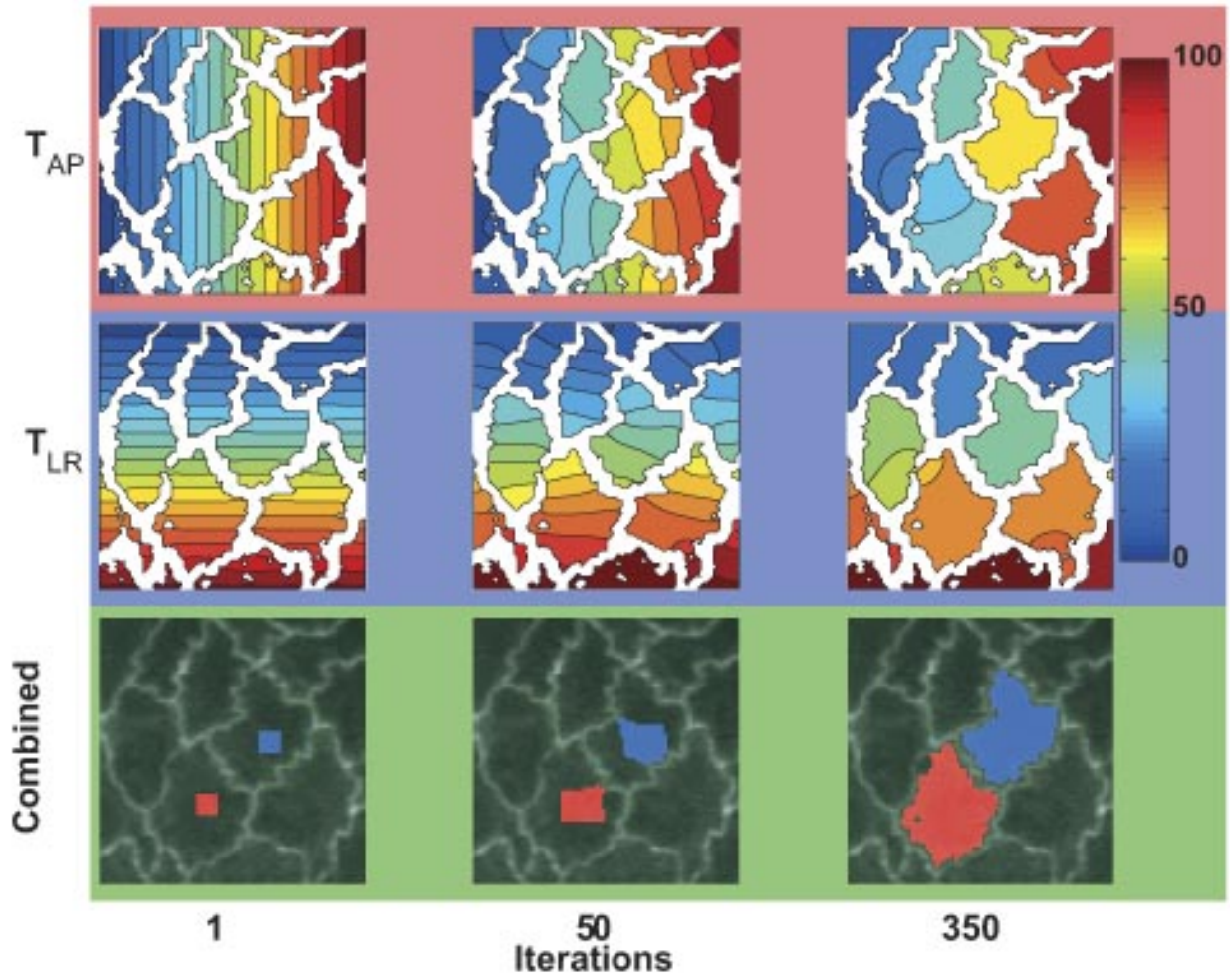

FIGURE S3. Implementation of the Seed Segmentation Algorithm: Left to right indicates the number of iterations of heat flow. The bottom row updates the segmentation of an open (red) and a closed (blue) cell, superimposed on a confocal image. The top row presents temperature contours in the assessment of an initial A-P temperature gradient, where black contour lines are separated by 5° and for presentation purposes the regions between the contour lines have been filled in with the average temperature values. The middle row presents an assessment of an initial L-R temperature gradient. False colors indicate temperature in degrees Celsius. Temperatures are considered to be common if they are within a user-defined temperature range, typically $5 - 15$°C. Typical data sets imaged the entire dorsal opening, where 4-8 patches of roughly 20-50 cells were processed sequentially with the net result being the segmentation of all amnioserosa cells in the confocal image. The reference to a region of interest in the flow chart of Figure (S2) refers to a patch of cells. This figure has been cropped for presentation purposes and therefore includes partial cells. The actual temperature distributions have been, in effect, digitized due to their presentation as a contour plot.

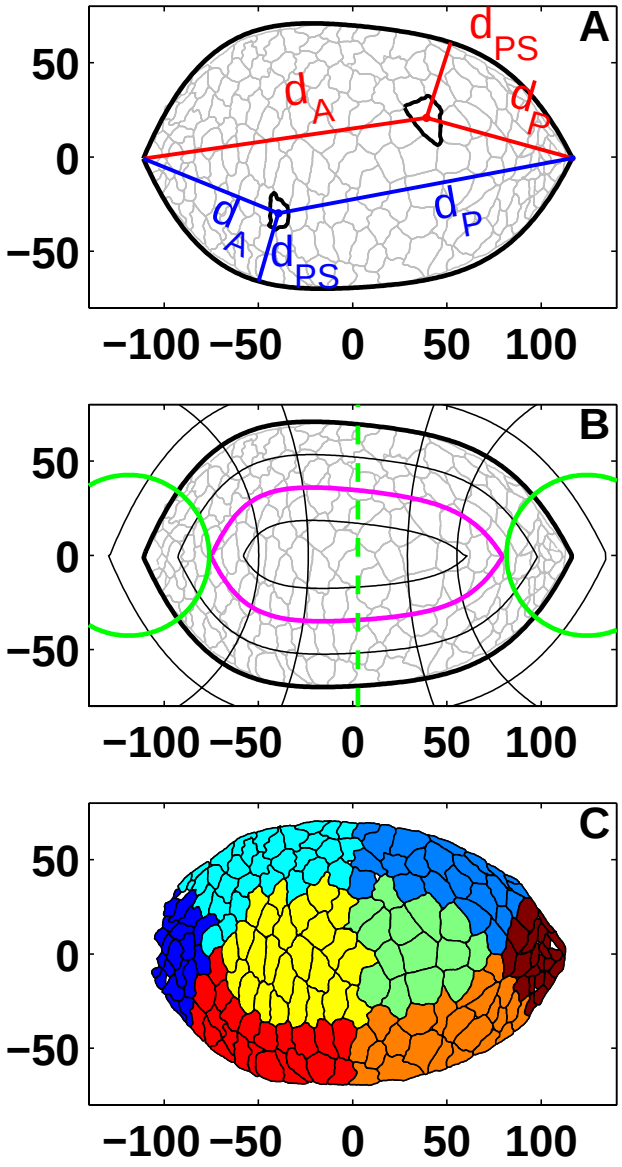

FIGURE S4. Characteristic distances and regionalization of the dorsal opening. *A*: Segmented amnioserosa cells shown in grey, the two purse strings shown in thick black, and the two intersections of the purse strings locate the two canthi. Two example cells highlight distance measurements from each cell centroid (red or blue) to the two canthi (d_A, d_P) and then the minimum distance to the closest leading edge (d_{LE}). *B*: Geometric construction of isocontours to regionalize the dorsal opening. The magenta isocontour is 35 microns from the nearest leading edge and the green isocontours are at values of -1.7, 0, and 1.7. *C*: Color scheme for regionalizing the dorsal opening.

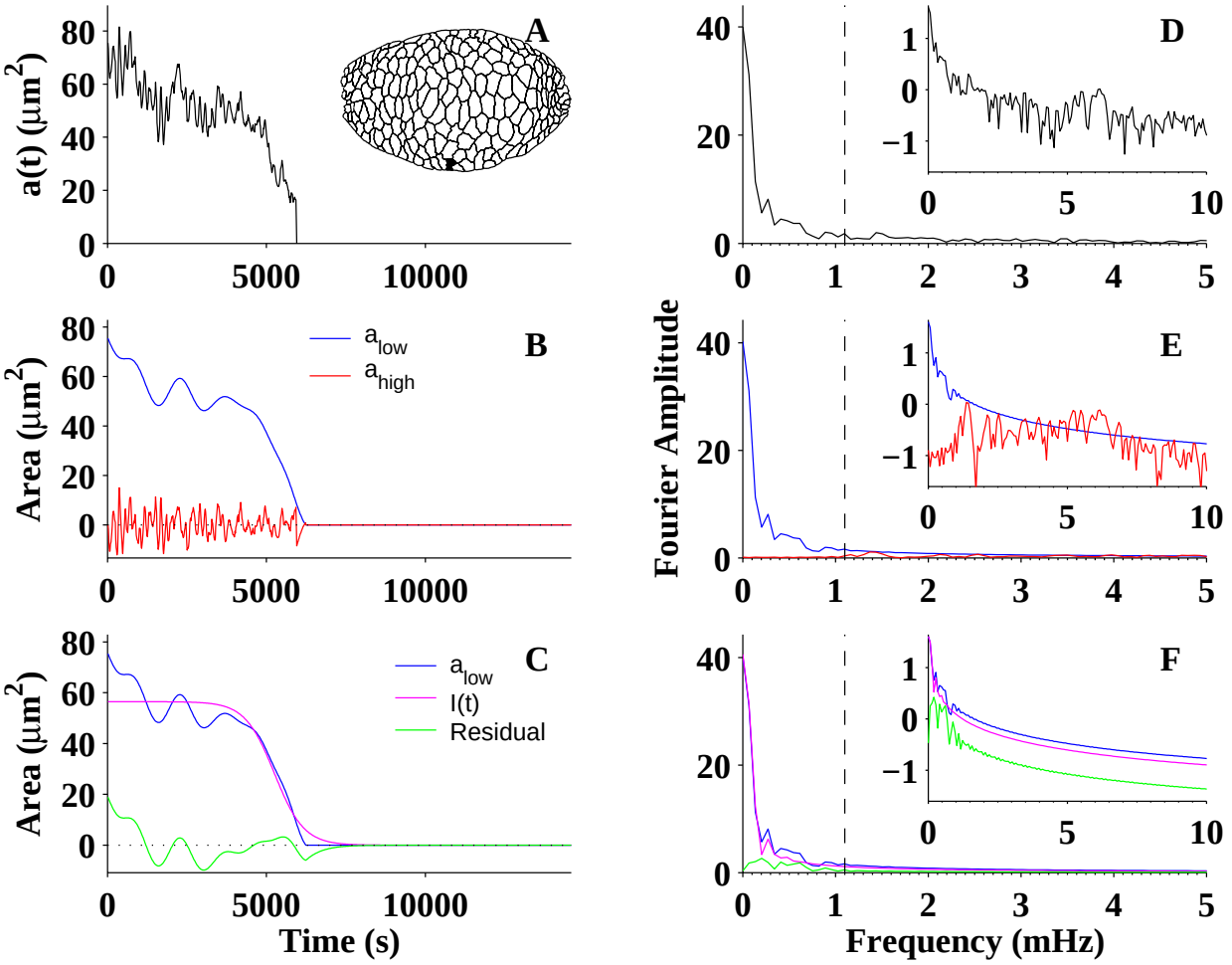

FIGURE S5. Signal analysis for a relatively fast delaminating cell (highlighted in the rendering of the embryo). Raw data (black) in the *A*: time and *D*: frequency domains. Low-frequency signal (blue) and high-frequency signal (red) in the *B*: time and *E*: frequency domains. $I_i(t)$ (purple) and low-frequency residual (green) in the *C*: time and *F*: frequency domains, where $a_{low,i}(t)$ and $\tilde{a}_{low,i}(\omega)$ (blue) traces, respectively, have been reproduced for comparison purposes. The insets in the right column are log-linear plots.

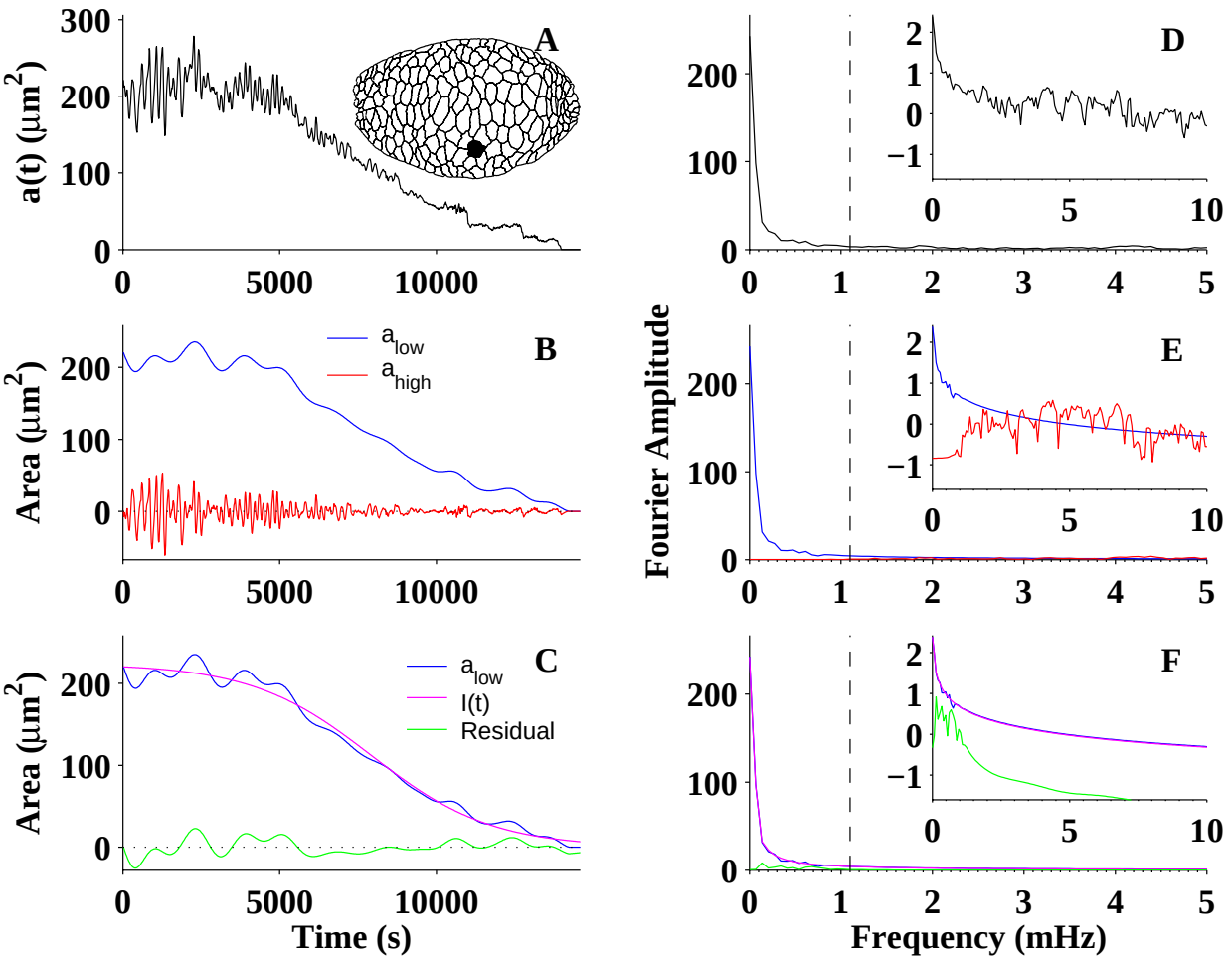

FIGURE S6. Signal analysis for a relatively slow and relatively large delaminating cell. See legend to Figure (S5) for details.

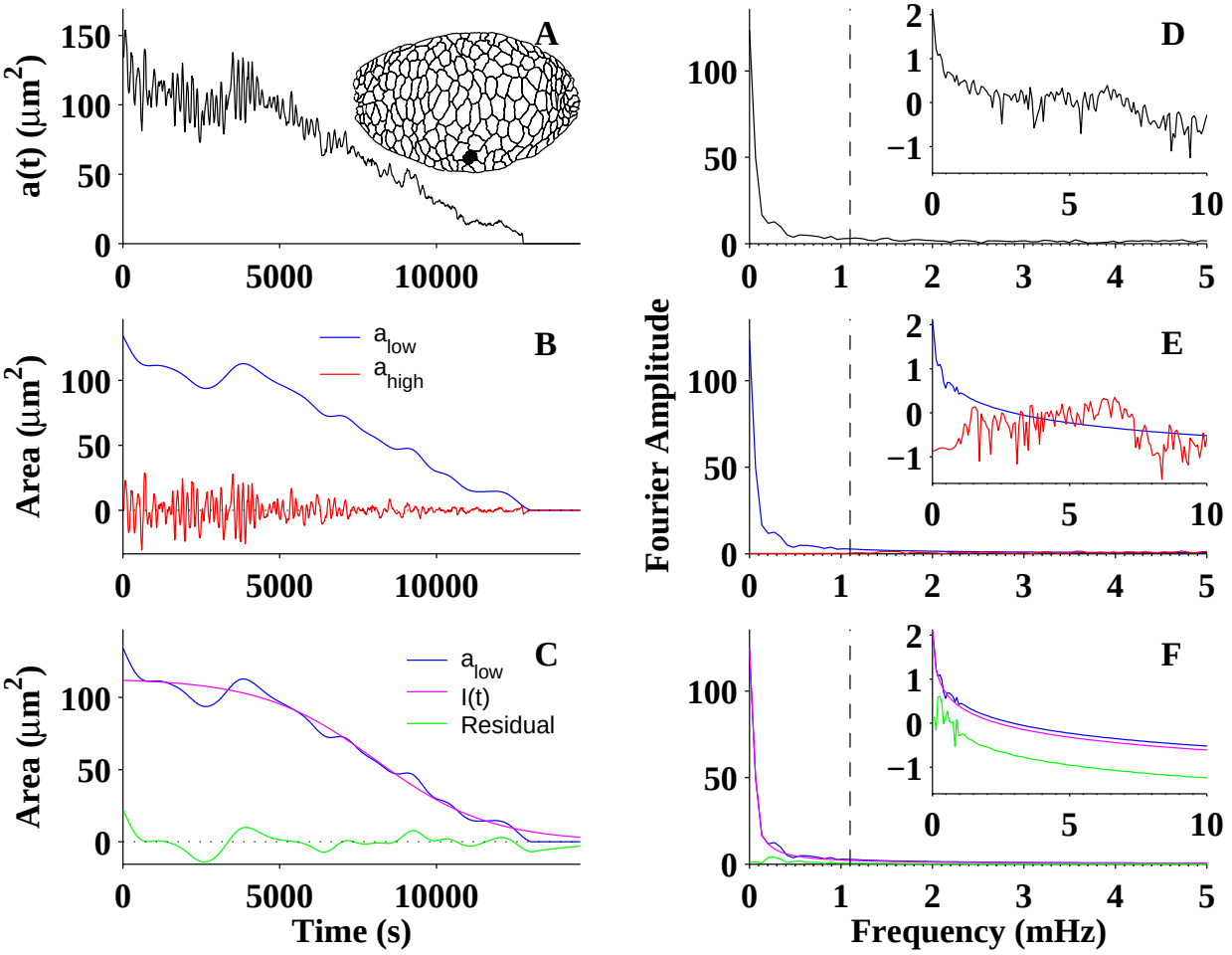

FIGURE S7. Signal analysis for a relatively slow and a relatively intermediately sized, delaminating cell. See legend to Figure (S5) for details.

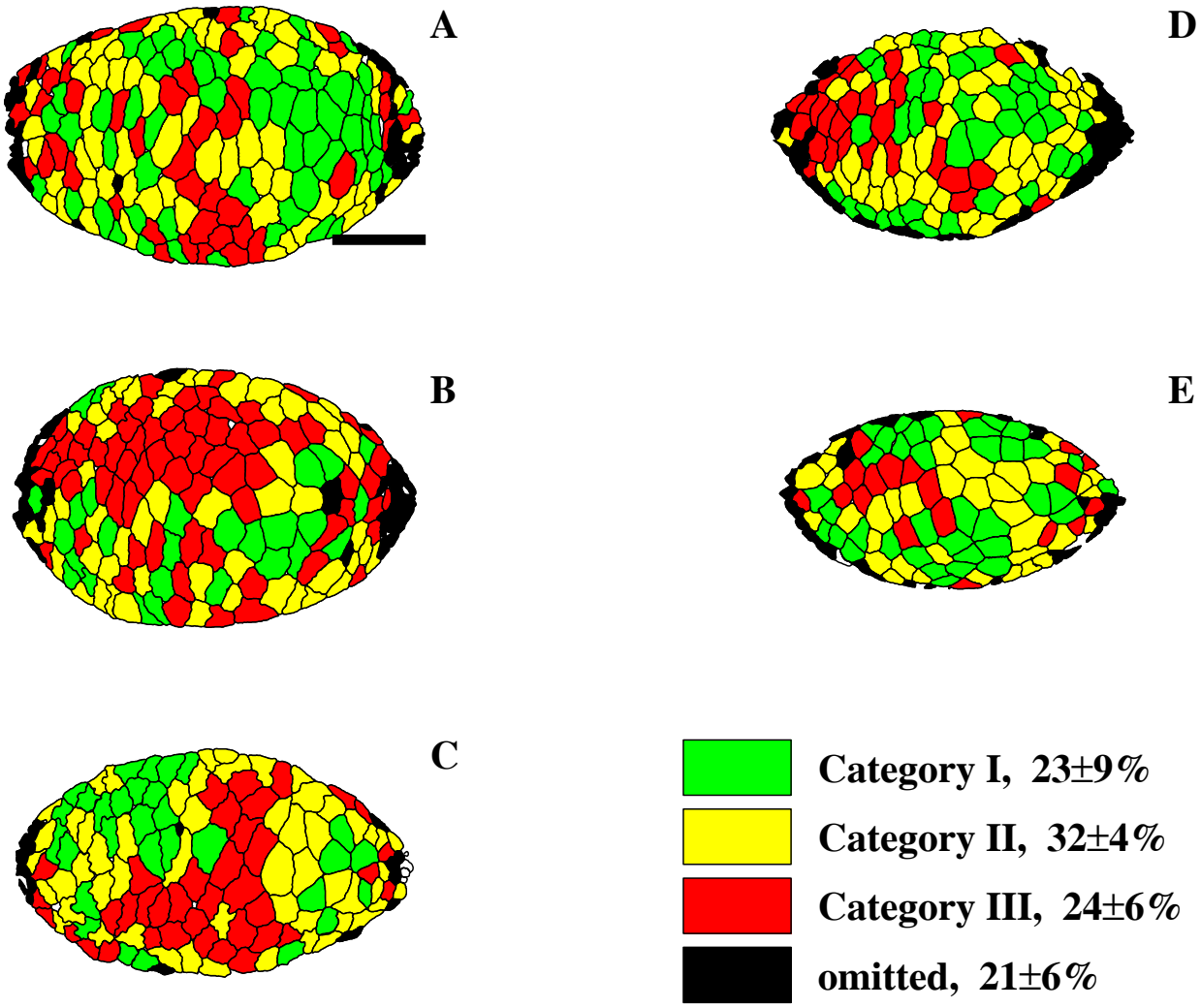

FIGURE S8. Distribution of category I, II, and III cells. Panels *A*-*E* correspond to the numbering scheme (1-5) for embryos as presented in Table (S1). Each embryo assessed at its initial confocal image. The color code for category values is presented in the lower right panel. Scale bar is 50 μm. The 170 black cells we "omitted" from this analysis.

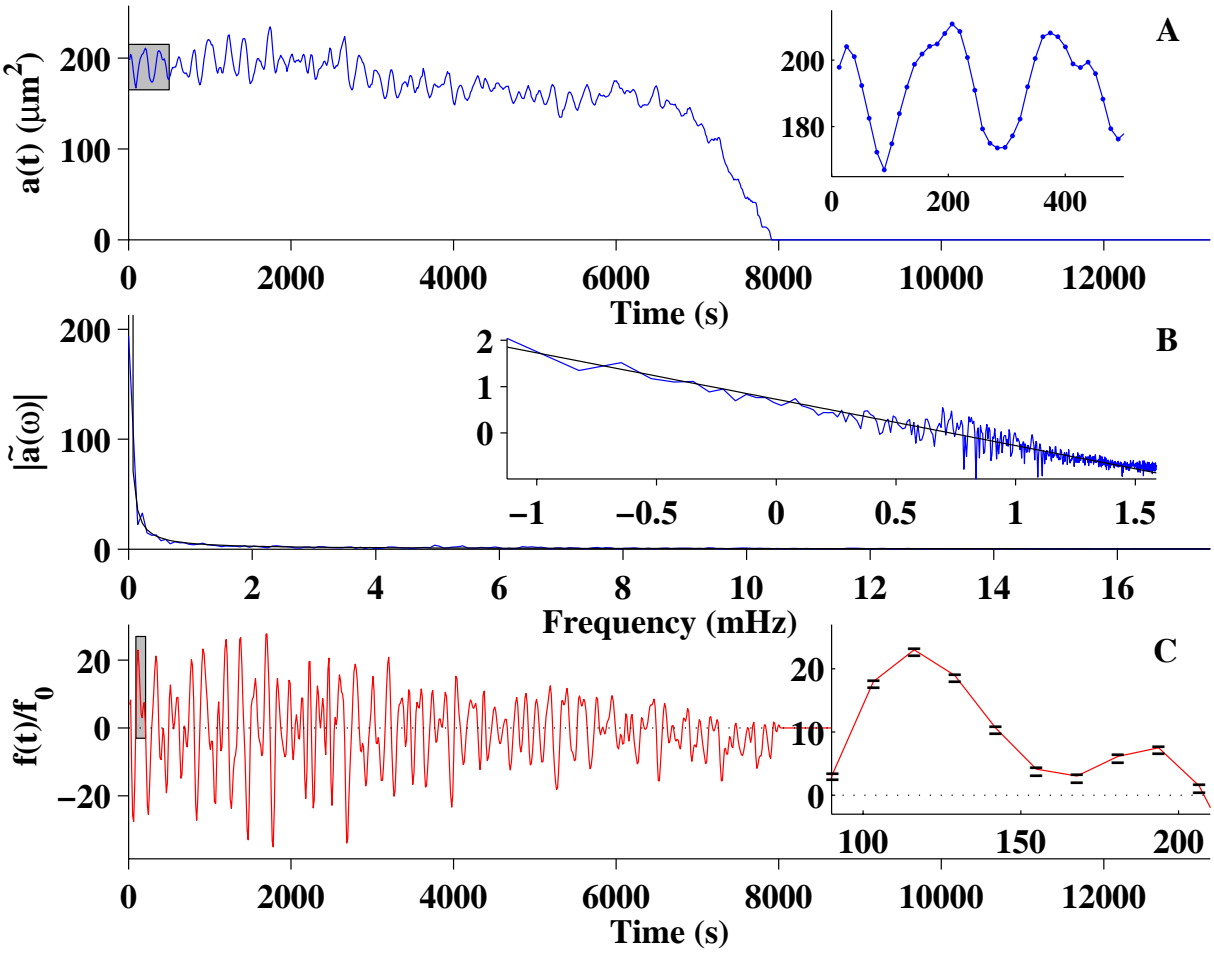

FIGURE S9. Viscoelastic analysis of cell apical area. *A*: Plot of $a_i(t)$ for a single cell (same cell as shown in Figure (2*A*-*D*)). The inset highlights the density of the data points from the grey region, well above the Nyquist limit. *B*: The Fourier transform of $a_i(t)$ from Panel *A*, where the inset exhibits the ω^{-1} dependence in a $\log - \log$ plot. *C*: The forcing function $f(t)/f_0$ calculated from Equation (S15) with fitting parameters $k_{eff}/b = 5 \times 10^{-5}$mHz and $f_0/b = 0.033 \mu m^2/s$. The inset summarizes the effect of varying k_{eff}/b from 0 to 4.5×10^{-4}mHz within the grey region.

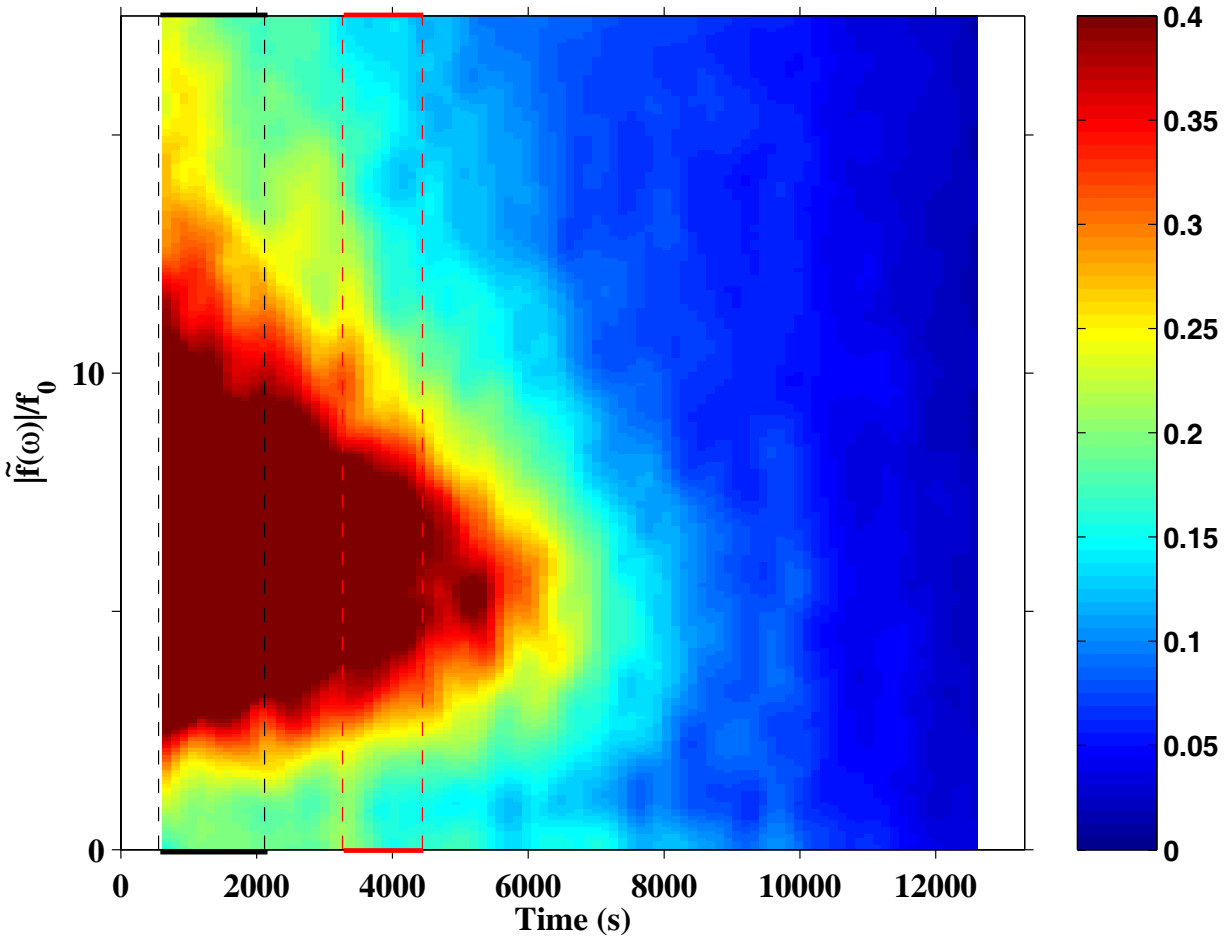

FIGURE S10. An alternative presentation of the data from Fig. 2*G* where the dynamic range of the false color scale is from 0 to 0.4 instead of 0 to 1. The x-axis reports time, the y-axis reports frequency, and the normalized amplitude is reported in the false color scale. The range in amplitudes is shortened on the false color scale to reveal the blue streak of ingression processes at lower frequencies. Note the streak at lowest frequencies from 1300 to $\sim$ 10000 seconds (compare this figure to Fig. 2*G*).

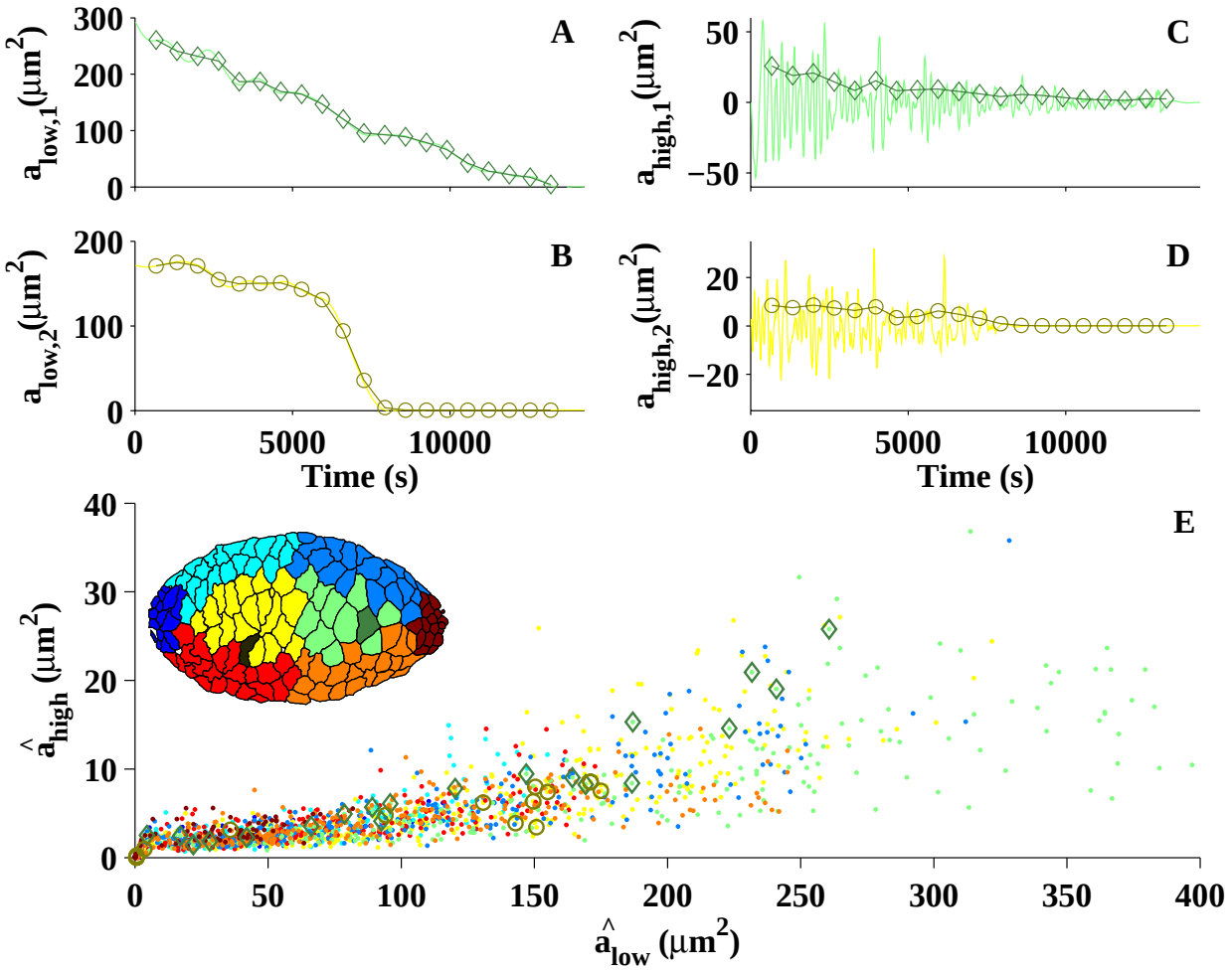

FIGURE S11. Amplitudes of high-frequency oscillations ($a_{high,i}$) correlate with background areas ($a_{low,i}$). All cells from embryo #3 were analyzed. The determination of average values for background areas (Panels *A* and *B*) and high-frequency oscillations (Panels *C* and *D*) are shown for two example cells. These example cells are indicated in the inset to Panel *E* (false colored regionalization of the dorsal opening, Supplement S1.4), where the cell from Panel *A* and *C* is from the posterior interior (green) region and highlighted in dark green in the inset. Similarly the yellow cell shown in Panels *B* and *D* is from the anterior interior (yellow) region and highlighted in brown in the inset. The diamonds in Panels *A* and *C* summarize the determination of values for the average background area ($\hat{a}_{low,i}$) and the average amplitudes of high-frequency oscillations ($\hat{a}_{high,i}$) for a linearly delaminating cell (Equations S17a and S17b, Supplement S1.3). Similarly the circles in Panels *B* and *D* summarize $\hat{a}_{low,i}$ and $\hat{a}_{high,i}$ for a relatively rapidly delaminating cell. Data for all the segmented cells are presented in Panel *E*, where the green diamonds and yellow circles highlight the two example cells. All the other cells are indicated by dots with colors corresponding to their regions. The average cell area exhibits a good linear correlation to the oscillation amplitude (166 cells of this embryo, $r^2 = 0.74$).

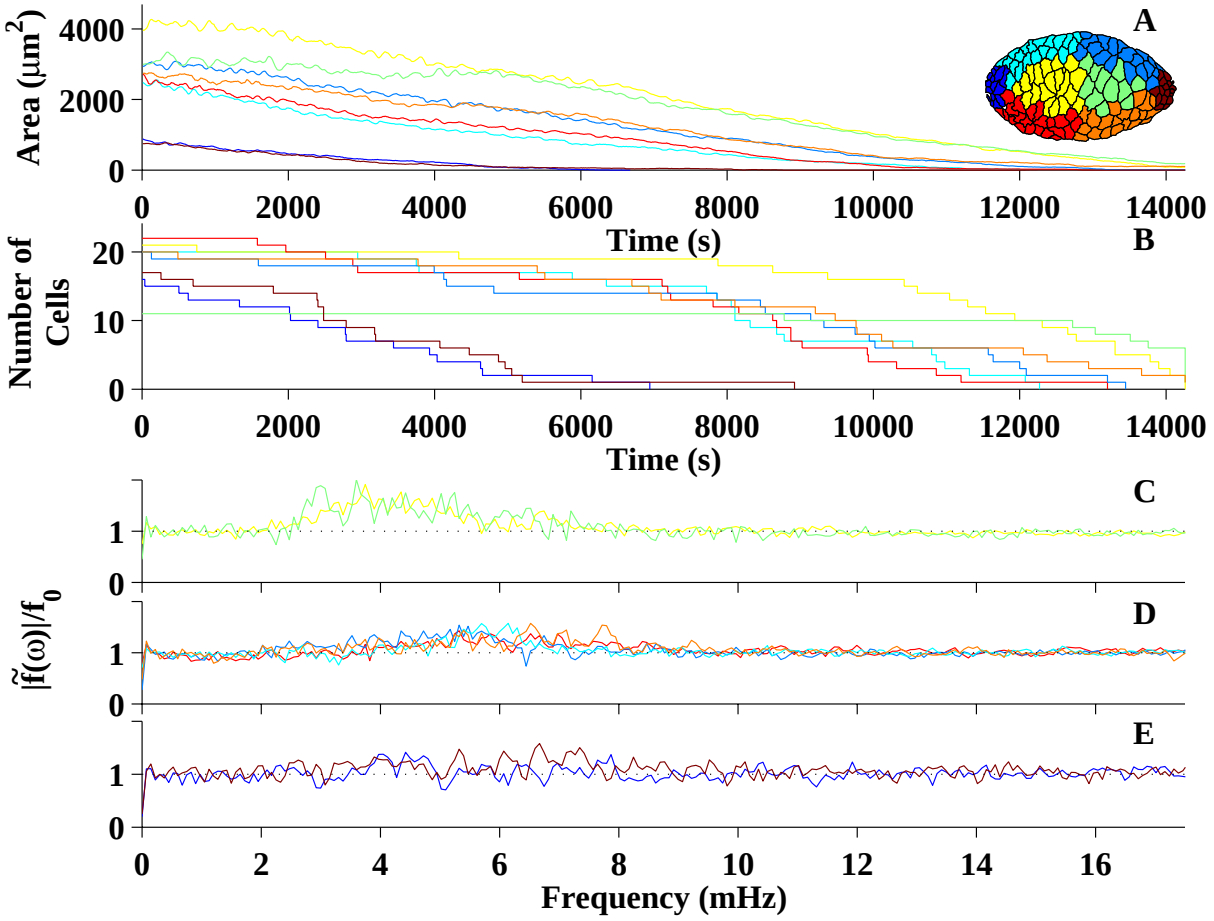

FIGURE S12. Regional analysis of amnioserosa cell ingression during dorsal closure (embryo #3). *A*: Plot of area as a function of time for the eight regions of the dorsal opening. The regions (see inset) fall into three groupings: the pole/canthus (dark blue, brown) regions, the central (yellow, green) regions, and the peripheral (cyan, red, blue, and orange) regions. *B*: Plots of the number of cells in each region as a function of time, where an amnioserosa cell is no longer counted once it completes the ingression process. *C*-*E*: The regional averages of the Fourier transform $|\tilde{f}_i(\omega)|/f_{0,i}$ of each forcing function $f_i(t)/b$ by region for all the segmented amnioserosa cells in one embryo, exhibiting similar groupings seen in panel *A*. Regional values for $f_{0,i}/b$ in units of $\mu m^2/s$: yellow region: 0.031 ± 0.006, green region: 0.038 ± 0.009, cyan region: 0.019 ± 0.005, red region: 0.019 ± 0.007, blue region: 0.025 ± 0.010, orange region: 0.021 ± 0.007, dark blue region: 0.015 ± 0.004 and brown region: 0.009 ± 0.002

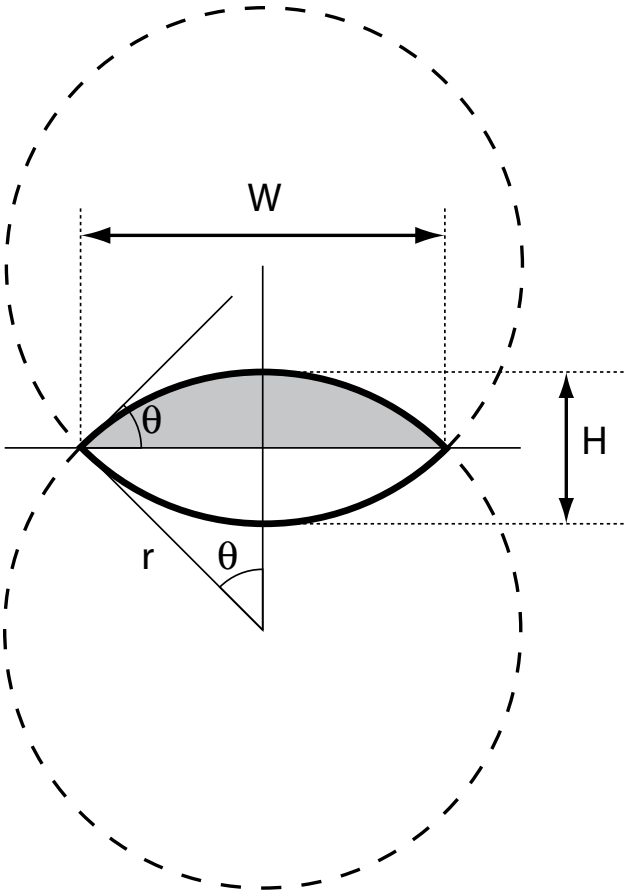

FIGURE S13. The common area between two intersecting circles defines the dorsal opening in the setting-sun model. Here r is the radius of the circle, H the largest purse-string-to-purse-string distance ($h = H/2$), and W is the distance between the two canthi ($w = W/2$).